



Vertical coupling and dynamical source for the intraseasonal variability in the deep Kuroshio Extension

Yang Yang¹ · X. San Liang² · Hideharu Sasaki³

Received: 6 April 2021 / Accepted: 24 August 2021 / Published online: 12 October 2021
© Springer-Verlag GmbH Germany, part of Springer Nature 2021

Abstract

In the power spectrum, the upper and deep parts of the Kuroshio Extension have distinctly different peaks. The former peaks around 200 days, while the latter is mainly at the intraseasonal band. How the upper meandering jet links the deep intraseasonal eddy current then makes an issue. In this study, it is investigated using the outputs from a $1/10^\circ$ ocean general circulation model. The theoretical framework is the theory of canonical transfer that gives a faithful representation of the energy transfers among distinct scales in the light of energy conservation, and a space-time-dependent energetics formalism with three-scale windows, namely, a slowly varying background flow window, an intraseasonal eddy window, and a high-frequency synoptic eddy window. The vertical pressure work is found to be the primary driver of the deep intraseasonal variability; it transports intraseasonal kinetic energy (IKE) to the deep layer (below 3000 m) from the interior layer (~ 200 – 3000 m) where the intraseasonal variability is generated through baroclinic instabilities. Besides the downward IKE fluxes, significant upward fluxes also exist in the surface mixed layer of the upstream Kuroshio Extension (above ~ 200 m, west of 146°E) as a comparable IKE source as baroclinic instability. The accumulated upstream IKE is advected eastward, forming the primary KE source of the intraseasonal variability in the surface layer of the downstream Kuroshio Extension (east of 146°E). Regarding the IKE sinks, the deep layer IKE is damped by bottom drag, while in the surface (interior) layer, IKE is damped by the wind stress and may also be given back to the background flow (the up/downward IKE fluxes via pressure work).

Keywords Kuroshio Extension · Intraseasonal variability · Baroclinic instability · Canonical transfer · Deep ocean

1 Introduction

As an inertial jet leaving from the Japan coast, the Kuroshio Extension is characterized by large amplitude meanders and vigorous mesoscale eddies. Thanks to the accumulating data

from satellite altimeter measurements and eddy-resolving numerical models, the past two decades have shown significant advancements in understanding of the large-scale and meso-scale oceanic variabilities in this region (Tai and White 1990; Qiu 1995; Qiu and Chen 2005; Taguchi et al. 2007; Greatbatch et al. 2010). For example, it is found that the Kuroshio Extension system exhibits a significant low-frequency (interannual-to-decadal) oscillation between a stable and an unstable state (Qiu and Chen 2005; Taguchi et al. 2007; Nonaka et al. 2020). During the unstable state, the jet takes a more meandering path which supports strong instabilities energizing the mesoscale variability (e.g., Qiu and Chen 2010; Yang et al. 2017; Wang et al. 2017) and vice versa. These progresses are mainly made in the upper layer circulation dynamics. In contrast, the deep circulation is less understood, owing to the lack of observations.

From 2004 to 2006, a multi-institutional collaborative project, namely, the Kuroshio Extension System Study (KESS), yielded an unprecedented dataset of current- and pressure-equipped inverted echo sounders (CPIES) moored in depths ranging from 5300 to 6400 m (Donohue et al. 2010). Several

Responsible Editor: Richard John Greatbatch

This article is part of the Topical Collection on *Atmosphere and Ocean Dynamics to celebrate the official retirement of Professor Dr. Richard J. Greatbatch*

✉ X. San Liang
sanliang@courant.nyu.edu

¹ School of Marine Sciences, and Center for Ocean-Atmosphere Dynamical Studies, Nanjing University of Information Science and Technology, Nanjing, China

² Department of Atmospheric and Oceanic Sciences and Institute of Atmospheric Sciences, Fudan University, Shanghai, China

³ Application Laboratory, Japan Agency for Marine-Earth Science and Technology, Yokohama, Japan

studies exploited this dataset to investigate the characteristics and dynamics of the deep circulation (e.g., Greene et al. 2009, 2012; Tracey et al. 2012; Bishop 2013; Na et al. 2016). They showed that significant variability exists in the intraseasonal band (periods of 30–60 days) at the abyssal Kuroshio Extension, mainly in the form of topographic Rossby waves (TRWs)(Greene et al. 2012; Miyamoto et al. 2017). These deep mesoscale signals are found to be jointly intensified with the upper layer meanders/eddies that drive large heat fluxes across the zonal jet (Bishop 2013). The vertical coupling between the deep and upper motions with the deep flows being shifted downstream with respect to the upper meander during their joint development period (Tracey et al. 2012; Greene et al. 2012; Bishop and Bryan 2013) reminds us of a classical scenario, that is, a scenario of baroclinic instability.

The instability property of the Kuroshio Extension system and associated temporal variation of the regional mesoscale eddy energy have been systematically addressed in a line of recent studies (Yang and Liang 2016; Yang et al. 2017; Yang and Liang 2018), with the implementation of a novel multiscale energetics in the framework of multiscale window transform (Liang 2016). From the viewpoint of long-term climatology, the eddy kinetic energy (EKE) in the upstream Kuroshio Extension is found to be generated by mixed baroclinic and barotropic instability that transfer energy toward the eddy flow from the available potential and kinetic energy of the background flow (Yang and Liang 2016). On the interannual-to-decadal time scale, the EKE variation is predominantly correlated with energy transfer due to barotropic instability of the meandering jet that modulates between the stable and unstable state (Yang et al. 2017). These energy transfer processes are found to be mainly confined within the upper ocean (Yang and Liang 2016). Up to now, little is known about the energy sources for the deep flow variability beneath the Kuroshio Extension jet. Additional insights need to be gained into the energy pathway by which the upper and deep layers are tightly linked as indicated by the observations (Bishop 2013).

The goal of this study is twofold: (1) to quantitatively depict the three-dimensional energy pathway in the whole water column of Kuroshio Extension based on an eddy-resolving global Ocean General Circulation Model for the Earth Simulator (OFES2) and (2) to clarify how the intraseasonal eddy energy in the deep ocean is connected with the upper. The paper is organized as follows: Section 2 describes the numerical model data and the energetics framework employed in this study; Section 3 presents the main results and section 4 presents a summary of the study.

2 Methods

2.1 Numerical model simulation

We use outputs from a global ocean model simulation to investigate the energetics at the intraseasonal time scale in the

Kuroshio Extension. The simulation is based on the Ocean General Circulation Model for the Earth Simulator version 2 (OFES2) which solves the Boussinesq, hydrostatic primitive equations on an Arakawa B-grid (Sasaki et al. 2020). The model has a horizontal resolution of $1/10^\circ$ from 76°S to 76°N and 105 vertical levels with grid spacing increasing from 5 m at the surface to 300 m near the bottom. It is initialized by the temperature and salinity fields obtained from an earlier version of OFES simulation (Sasaki et al. 2008) on January 1, 1958, with no motion, and is forced by the 3-hourly atmospheric surface dataset JRA55-do v08 (Tsujino et al., 2018). The air-sea fluxes are calculated using the bulk formula by Large and Yeager (2004). In order to include the feedback of oceanic currents to the wind stress, the wind speed relative to the surface current is considered in the surface momentum flux estimation. River outflow is implemented as a freshwater flux using the monthly mean climatological river runoff dataset from Coordinated Ocean–Ice Reference Experiments (CORE) version 2 (Large and Yeager 2004). Vertical mixing is implemented with mixed layer vertical mixing scheme of a second-order turbulence closure model developed by Noh and Kim (1999) and a local tidal mixing scheme developed by Jayne and Laurent (2001) and St. Laurent et al. (2002). A biharmonic horizontal mixing scheme is used with a viscosity of $2.7 \times 10^{10} \text{ m}^4 \text{ s}^{-1}$ and a diffusivity of $9 \times 10^9 \text{ m}^4 \text{ s}^{-1}$. The outputs from this simulation have been thoroughly evaluated and compared against observations in Sasaki et al. (2020). Since no data assimilation constrains the forward integration, outputs from this free-run simulation are dynamically consistent and thus suitable for the following dynamical analysis. The daily snapshots from 1 Jan 1993 to 31 Dec 2009 are used for the present study. Since the model output fields are on a B-grid, they have been linearly interpolated onto the same horizontal and vertical grids before the energetics diagnosis is performed.

2.2 Multiscale energetics

Oceanic processes tend to occur on a range of scales, or scale windows, as termed by Liang and Anderson (2007). To investigate the dynamical processes responsible for the generation and redistribution of the intraseasonal variability in the Kuroshio Extension, we define three temporal scale windows, namely, a low-frequency background flow window, an intraseasonal eddy window, and a high-frequency eddy window. We use the multiscale window transform (MWT), developed by Liang and Anderson (2007), to fulfill the scale separation. MWT is a functional analysis tool that orthogonally decomposes a function space into a direct sum of scale windows. Given a time series $u(t)$, if we consider a three-

scale window decomposition, u can be reconstructed onto three windows:

$$u(t) = \sum_{\varpi=0}^2 u^{\sim\varpi}(t), \tag{1}$$

with the notations $\varpi = 0, 1,$ and $2,$ respectively, signifying the background flow window, intraseasonal eddy window, and high-frequency eddy window. $u^{\sim\varpi}(t)$ is the reconstruction of u on window ϖ which is defined by:

$$u^{\sim\varpi}(t) = \sum_{n=0}^{2^{j_2-1}} \hat{u}_n^{\sim\varpi} \phi_n^{j_2}(t), \tag{2}$$

where

$$\hat{u}_n^{\sim\varpi} = \int_0^1 u^{\sim\varpi}(t) \phi_n^{j_2}(t) dt, \tag{3}$$

$\phi(t)$ is a localized scaling basis, j is the wavelet scale level and n is the discrete time step in the sampling space. Equations

(2) and (3) are the multiscale window reconstruction (MWR) and its peer, MWT, respectively. For each MWR of a time series $u(t), u^{\sim\varpi}(t),$ there is a corresponding transform coefficient, denoted as $\hat{u}_n^{\sim\varpi}.$ The *time-dependent* energy on window ϖ proves to be the square of the transform coefficients, i.e., $(\hat{u}_n^{\sim\varpi})^2$ (up to some constant; cf. Liang and Anderson 2007). Note that it is by no means trivially the square of the reconstructed (filtered) field, i.e., $[u^{\sim\varpi}(t)]^2,$ as commonly used in the literature. For more details on the multiscale energy presentation, refer to the [appendix](#).

By applying MWT to the momentum and density equations, Liang (2016) obtained the equations governing the rate of change of kinetic energy (KE) on window ϖ (denoted as K^ϖ) and available potential energy (APE) on window ϖ (denoted as A^ϖ):

$$\begin{aligned} \frac{\partial K^\varpi}{\partial t} = & \underbrace{\frac{1}{2} [(\widehat{\mathbf{v}\mathbf{v}_h})^{\sim\varpi} : \nabla \widehat{\mathbf{v}}_h^{\sim\varpi} - \nabla \cdot (\widehat{\mathbf{v}\mathbf{v}_h})^{\sim\varpi} \cdot \widehat{\mathbf{v}}_h^{\sim\varpi}]}_{\Gamma_K^\varpi} + \underbrace{\left\{ -\nabla \cdot \left[\frac{1}{2} (\widehat{\mathbf{v}\mathbf{v}_h})^{\sim\varpi} \cdot \widehat{\mathbf{v}}_h^{\sim\varpi} \right] \right\}}_{\Delta Q_K^\varpi} \\ & + \underbrace{\left[-\nabla_h \cdot \left(\frac{1}{\rho_0} \widehat{\mathbf{v}}_h^{\sim\varpi} \widehat{P}^{\sim\varpi} \right) \right]}_{\Delta_h Q_P^\varpi} + \underbrace{\left[-\frac{\partial}{\partial z} \left(\frac{1}{\rho_0} \widehat{w}^{\sim\varpi} \widehat{P}^{\sim\varpi} \right) \right]}_{\Delta_z Q_P^\varpi} + \underbrace{\left(-\frac{\mathbf{g}}{\rho_0} \widehat{\rho}_a^{\sim\varpi} \widehat{w}^{\sim\varpi} \right)}_{b^\varpi} + F_K^\varpi, \tag{4} \end{aligned}$$

$$\begin{aligned} \frac{\partial A^\varpi}{\partial t} = & \underbrace{\frac{c}{2} [(\widehat{\mathbf{v}\rho_a})^{\sim\varpi} \cdot \nabla \widehat{\rho}_a^{\sim\varpi} - \widehat{\rho}_a^{\sim\varpi} \nabla \cdot (\widehat{\mathbf{v}\rho_a})^{\sim\varpi}]}_{\Gamma_A^\varpi} + \underbrace{\left\{ -\nabla \cdot \left[\frac{1}{2} c \widehat{\rho}_a^{\sim\varpi} (\widehat{\mathbf{v}\rho_a})^{\sim\varpi} \right] \right\}}_{\Delta Q_A^\varpi} \\ & + \underbrace{\left(\frac{\mathbf{g}}{\rho_0} \widehat{\rho}_a^{\sim\varpi} \widehat{w}^{\sim\varpi} \right)}_{-b^\varpi} + \underbrace{\frac{1}{2} \widehat{\rho}_a^{\sim\varpi} (\widehat{w\rho_a})^{\sim\varpi} \frac{\partial c}{\partial z}}_{S_A^\varpi} + F_A^\varpi, \tag{5} \end{aligned}$$

where $K^\varpi = (\widehat{\mathbf{v}}_h^{\sim\varpi} \cdot \widehat{\mathbf{v}}_h^{\sim\varpi}) / 2$ and $A^\varpi = c(\widehat{\rho}_a^{\sim\varpi})^2 / 2$ are, respectively, the time-dependent multiscale KE and APE; \mathbf{v} and ∇ are, respectively, the three-dimensional velocity and gradient operator; and those with subscript h denote their horizontal counterparts; ρ_a is the density perturbation from a stationary reference state $\bar{\rho}(z)$ (time- and area-mean density at each depth); P is the dynamic pressure field related to ρ_a ; $c = g^2 / \rho_0^2 N^2, N = \sqrt{-(g/\rho_0) d\bar{\rho}/dz}$ is the buoyancy frequency; and $(:)$ is the colon (double dot) product of two dyads (cf. Liang 2016). The other notations are conventional.

On the right-hand sides of Eqs. (4) and (5), the ΔQ_K^ϖ (ΔQ_A^ϖ) term represents the nonlocal transport of K^ϖ (A^ϖ) induced by advection; ΔQ_P^ϖ is another nonlocal process induced by

pressure work and is split into horizontal ($\Delta_h Q_P^\varpi$) and vertical ($\Delta_z Q_P^\varpi$) components because the vertical pressure work has been previously found to be essential to couple the eddy energetics between the upper and deep layer in the ocean (Zhai and Marshall 2012; Yang et al. 2020; Maslo et al. 2020). Physically, ΔQ_P^ϖ represents the rate of work done by the pressure fluctuations on scale window ϖ . This process has long been recognized as an important mechanism for the spatial redistribution of EKE both in the atmosphere (e.g., Mak and Cai 1988; Holmes and Thomas 2016) and the ocean (e.g., Dewar and Bane 1989; Chapman et al. 2015). Most of these studies focus on the impact of pressure work on the horizontal EKE redistribution. The potential role of pressure work on the

vertical eddy energy transport in the ocean is not well-studied until Zhai and Marshall (2012)’s work. They found distinctly different vertical pressure flux patterns in the North Atlantic subtropical and subpolar gyres, i.e., downward (upward) flux in the subtropical (subpolar) gyre. Later, we will show that a downward pressure flux exists in the Kuroshio Extension, similar to that discovered in the western boundary of the North Atlantic subtropical gyre (Zhai and Marshall 2012), which seems to indicate a universal mechanism that the eddy energy in the deep ocean is supplied through pressure work from the upper layer (Wunsch and Ferrari 2004). The b^ϖ term is the buoyancy conversion from A^ϖ to K^ϖ . S_A^ϖ is an apparent source/sink of A^ϖ due to the nonlinearity of the reference stratification and is usually negligible for mesoscale energetics. The F_K^ϖ (F_A^ϖ) term represents all of the effects of external forcing (such as wind/bottom stress) and frictional dissipation and are treated as the residue of the respective budget equation in this study. Mostly importantly, Γ_K^ϖ (Γ_A^ϖ) is the cross-scale energy transfer that measures the KE (APE) transferred from other windows toward window ϖ . Both transfer matrices satisfy an important property:

$$\sum_{\varpi} \sum_n \Gamma_n^\varpi = 0, \tag{6}$$

where \sum_{ϖ} and \sum_n are the summation over all the sampling time steps n and scale windows ϖ , respectively. This conservation property, which is not met in classical energetics formalisms, states that Γ only redistributes energy in phase (frequency) space, without generating or consuming energy as a whole. To distinguish, Γ is termed ‘‘canonical transfer’’ (Liang 2016). More details about canonical transfer are provided in the Appendix.

Note that the canonical transfer matrices (i.e., Γ_K^ϖ and Γ_A^ϖ) in Eqs. (4) and (5) need to be further decomposed to obtain the window-to-window interactions embedded in the three-scale window framework. Technical details are referred to Liang and Robinson (2005). Here, we use superscript like $0 \rightarrow 1$ to signify such interactions. For instance, the canonical transfer of KE (APE) from the background flow window ($\varpi = 0$) to the intraseasonal eddy window ($\varpi = 1$) is denoted as $\Gamma_K^{0 \rightarrow 1}$ ($\Gamma_A^{0 \rightarrow 1}$). A positive $\Gamma_K^{0 \rightarrow 1}$ ($\Gamma_A^{0 \rightarrow 1}$) means a release of background flow KE (APE) for the growth of intraseasonal variability, which is associated with barotropic (baroclinic) instability (Liang and Robinson 2007). Similarly, the scale interaction between the synoptic eddy and the intraseasonal eddy is quantified by $\Gamma_K^{2 \rightarrow 1}$ and $\Gamma_A^{2 \rightarrow 1}$. A positive $\Gamma_K^{2 \rightarrow 1}$ ($\Gamma_A^{2 \rightarrow 1}$) means an inverse temporal cascade of KE (APE) from the high-frequency eddies to the intraseasonal eddies. These canonical transfer matrices, localized both in time and space, allow us to quantify the spatio-temporal variations of the multiscale interactions in the Kuroshio Extension.

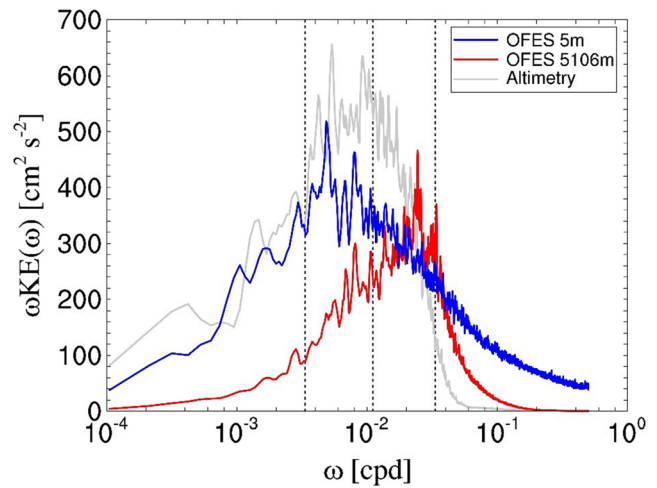


Fig. 1 The frequency spectra of KE averaged over the upstream region of Kuroshio Extension (32°–38°N, 142°–150°E). The spectra are plotted in variance-preserving form (i.e., multiplied by frequency ω). The blue and red curves are estimated from the total velocity fields at 5 m and 5106 m from OFES2, respectively. The gray curve is estimated from the geostrophic velocity fields from the daily gridded satellite altimetry sea surface height product distributed by the Copernicus Marine and Environment Monitoring Service (CMEMS). The values of the red curve have been multiplied by 30 to be plotted with the same ordinate. The dashed vertical lines from left to right denote the periods of 300, 90 and 30 days, respectively. All spectra are calculated for the period from 1 Jan 1993 to 31 Dec 2009

3 Results

3.1 Intraseasonal eddy kinetic energy in the Kuroshio Extension

Fig. 1 displays the KE power spectra at the surface (red line) and deep (blue line) Kuroshio Extension estimated from the OFES2 simulation. The frequency spectrum of KE is computed as $KE(\omega) = (1/2)\widehat{\mathbf{v}}_h \cdot \widehat{\mathbf{v}}_h^*$, where ω denotes frequency, $\widehat{\mathbf{v}}_h$ denotes the Fourier transform of the horizontal velocity vector \mathbf{v}_h at some depth, and the superscript * signifies complex conjugate. It can be seen that the spectral content of KE for the two layers are remarkably different. For the deep layer (red curve), the energy is largely confined to the 30–90-day (i.e., intraseasonal) band and has peaks around 40 days, consistent with the KESS observation (Greene et al. 2012; Bishop and Bryan 2013). In contrast, in the surface layer (blue curve), the KE peaks are shifted to periods longer than 90 days with energy concentrated around 200 days. Similar spectral shape with peaks around 200 days is also found in the spectrum inferred from satellite altimetry (gray curve in Fig. 1). Notice that the simulated KE level in the mesoscale (30–300 day) band is lower than that estimated from the satellite observation. This is likely due to the model’s incorporation of relative velocity in the wind stress estimation, which induces a significant damping of EKE (Renault et al. 2020; Sasaki et al.,

Fig. 2 Time-mean (1993–2009) maps of intraseasonal KE (K^1 ; $10^{-3} \text{ m}^2 \text{ s}^{-2}$) at (a) 5 m and (b) 5106 m. Black contours denote the mean sea surface height. Blue contours in (a) denote the 2000-, 3000-, 4000-, and 5000-m isobaths. Blue contours in (b) denote the isobath of 5106 m. The two gray-outlined rectangles, marked as 1 and 2, respectively, indicate the upstream region (i.e., $32^\circ\text{--}38^\circ\text{N}$, $142^\circ\text{--}146^\circ\text{E}$) and downstream region ($32^\circ\text{--}38^\circ\text{N}$, $146^\circ\text{--}155^\circ\text{E}$) in which area-integrated/averaged energetics are calculated in Section 3c

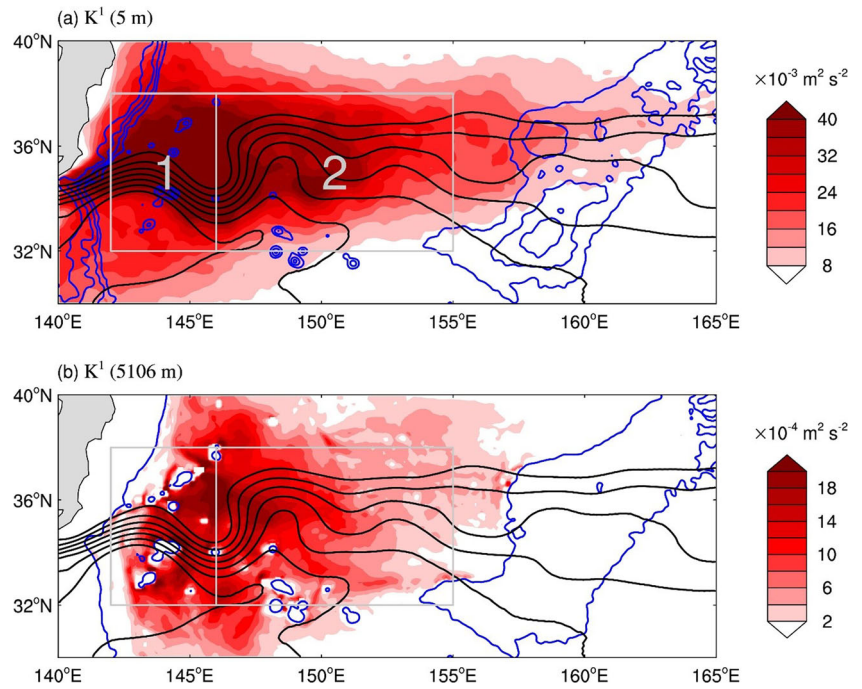
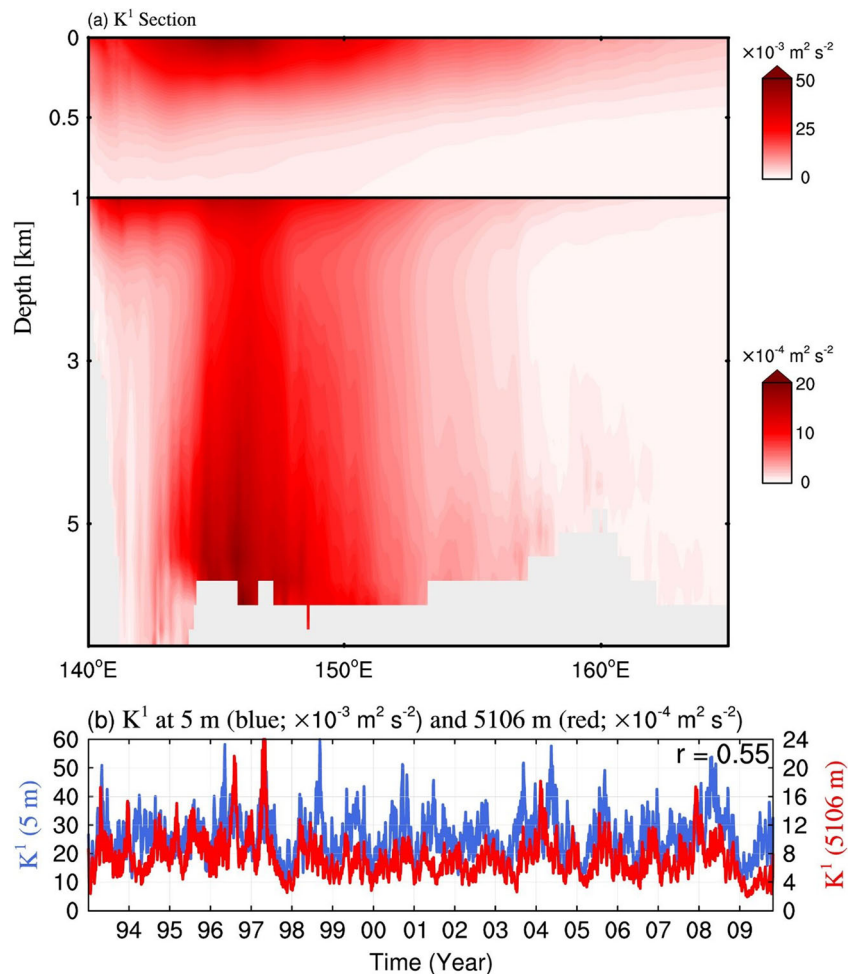


Fig. 3 Time-mean (1993–2009) depth-longitude sections of K^1 ($10^{-3} \text{ m}^2 \text{ s}^{-2}$) averaged along the $32^\circ\text{--}38^\circ\text{N}$ band. Note that the z -axis is not linear and the color scales above and below 1000 mare different. (c) Time series of K^1 averaged over the region of $32^\circ\text{--}38^\circ\text{N}$, $142^\circ\text{--}155^\circ\text{E}$ at (a) 5 m (blue) and (b) 5106 m (red)



2020). Another possible reason could be that the 1/10° OFES2 model does not resolve submesoscale processes, which have been found to energize the mesoscale flows through significant inverse energy cascades down to the mixed layer Rossby radius (Qiu et al. 2014; Sasaki et al. 2014).

In order to investigate the energy sources/sinks for the deep mesoscale variability whose energy as previously shown is confined to the intraseasonal band, we perform a three-scale window decomposition with MWT. For example, a flow field variable can be decomposed into three components, a low-frequency background flow (periods longer than 90 days; including the mean current and low-frequency mesoscale motions), an intraseasonal (periods between 30 and 90 days) flow, and a high-frequency (synoptic scale) flow (periods shorter than 30 days). Note that the synoptic scale motions are not well-captured by the altimetry observation but are present in the OFES2 simulation (Fig. 1). The impact of these high-frequency motions to the intraseasonal variability is yet to be explored. For easy reference, we use $\varpi = 0, 1, 2$ to indicate these three windows.

Fig. 2a and 2b show the long-term mean horizontal distributions of the intraseasonal KE (K^1) at depths of 5 m and 5106 m, respectively. The surface K^1 is maximized in the two quasi-stationary meanders and decays gradually to the east, while the deep K^1 is confined in a smaller area beneath the meanders due to the constraint of bathymetry. The vertical structure reveals that K^1 is surface intensified and decays remarkably with depth in the upper 1000 m (Fig. 3a). Below 1500 m, although small in amplitude, K^1 gradually increases with depth and exhibits a secondary maximum at depth around 5000 m (Fig. 3a). The bottom intensified structure of the abyssal currents in the Kuroshio Extension region is also reported in previous studies based on observation records (e.g., Bishop et al. 2012). Note that the strongest K^1 in the deep layer occurs between 144° and 145°E which is well beneath the upper meander trough where the K^1 level is highest, suggesting a possible vertical coupling between the upper and deep layers.

To confirm this, we plot the time series of K^1 at depths of 5 m and 5106 m in Fig. 3b. The two time series are significantly correlated (correlation coefficient of 0.55), indicating that the intraseasonal processes in the upper and deep layers are closely connected in this region.

3.2 Intraseasonal-scale energy generation and dissipation

In the following, we focus on the energy sources and sinks for the mesoscale variability within the intraseasonal band, aiming to understand how the dynamics in the upper and deep layers are coupled. For easy reference, the budget equations for K^1 and A^1 are symbolically written as follows:

$$\frac{\partial K^1}{\partial t} = \Gamma_K^{0 \rightarrow 1} + \Gamma_K^{2 \rightarrow 1} + b^1 + \Delta Q_K^1 + \Delta_h Q_P^1 + \Delta_z Q_P^1 + F_K^1, \text{ and} \tag{7}$$

$$\frac{\partial A^1}{\partial t} = \Gamma_A^{0 \rightarrow 1} + \Gamma_A^{2 \rightarrow 1} - b^1 + \Delta Q_A^1 + S_A^1 + F_A^1, \tag{8}$$

where the physical meanings of the terms are summarized in Table 1. Fig. 4 and 5 show the time-mean depth-longitude distributions of the A^1 and K^1 budget terms. These quantities have been meridionally averaged between 32°N and 38°N, which bounds the jet meanders where highest K^1 is observed. The upper A^1 budget is dominantly balanced by large amplitude positive $\Gamma_A^{0 \rightarrow 1}$ (i.e., $A^0 \rightarrow A^1$; Fig. 4a) and negative $-b^1$ (i.e., $A^1 \rightarrow K^1$; Fig. 4c). That is to say, the APE stored in the low-frequency background flow is released to the intraseasonal variability, and then converted to intraseasonal EKE, showing a typical baroclinic instability energy pathway in the ocean (e.g., Pedlosky 1987; von Storch et al. 2012). From Fig. 4a to 4c, we can see that the canonical APE transfer and buoyancy conversion can extend to a depth of ~3000 m in the upstream region.

Table 1 Physical meaning of the energy terms in Eqs. (7) and (8)

Symbol	Meaning	Symbol	Meaning
$\Gamma_K^{0 \rightarrow 1}$	Canonical KE transfer from background flow window ($\varpi = 0$) to intraseasonal-scale window ($\varpi = 1$)	$\Gamma_A^{0 \rightarrow 1}$	Canonical APE transfer from background flow window ($\varpi = 0$) to intraseasonal-scale window ($\varpi = 1$)
$\Gamma_K^{2 \rightarrow 1}$	Canonical KE transfer from synoptic scale window ($\varpi = 2$) to intraseasonal-scale window ($\varpi = 1$)	$\Gamma_A^{2 \rightarrow 1}$	Canonical APE transfer from synoptic scale window ($\varpi = 2$) to intraseasonal-scale window ($\varpi = 1$)
ΔQ_K^1	KE spatial transport on intraseasonal-scale window	ΔQ_A^1	APE spatial transport on intraseasonal-scale window
$\Delta_h Q_P^1$	Horizontal pressure work on intraseasonal-scale window	b^1	Buoyancy conversion on intraseasonal-scale window. Positive b^1 means a conversion from intraseasonal-scale APE to intraseasonal-scale KE
$\Delta_z Q_P^1$	Vertical pressure work on intraseasonal-scale window	S_A^1	Apparent source/sink of APE that is due to the nonlinearity of the reference stratification on intraseasonal-scale window
F_K^1	Change rate of KE due to wind stress and internal dissipation on intraseasonal-scale window	F_A^1	Change rate of APE due to buoyancy flux and diffusion on intraseasonal-scale window

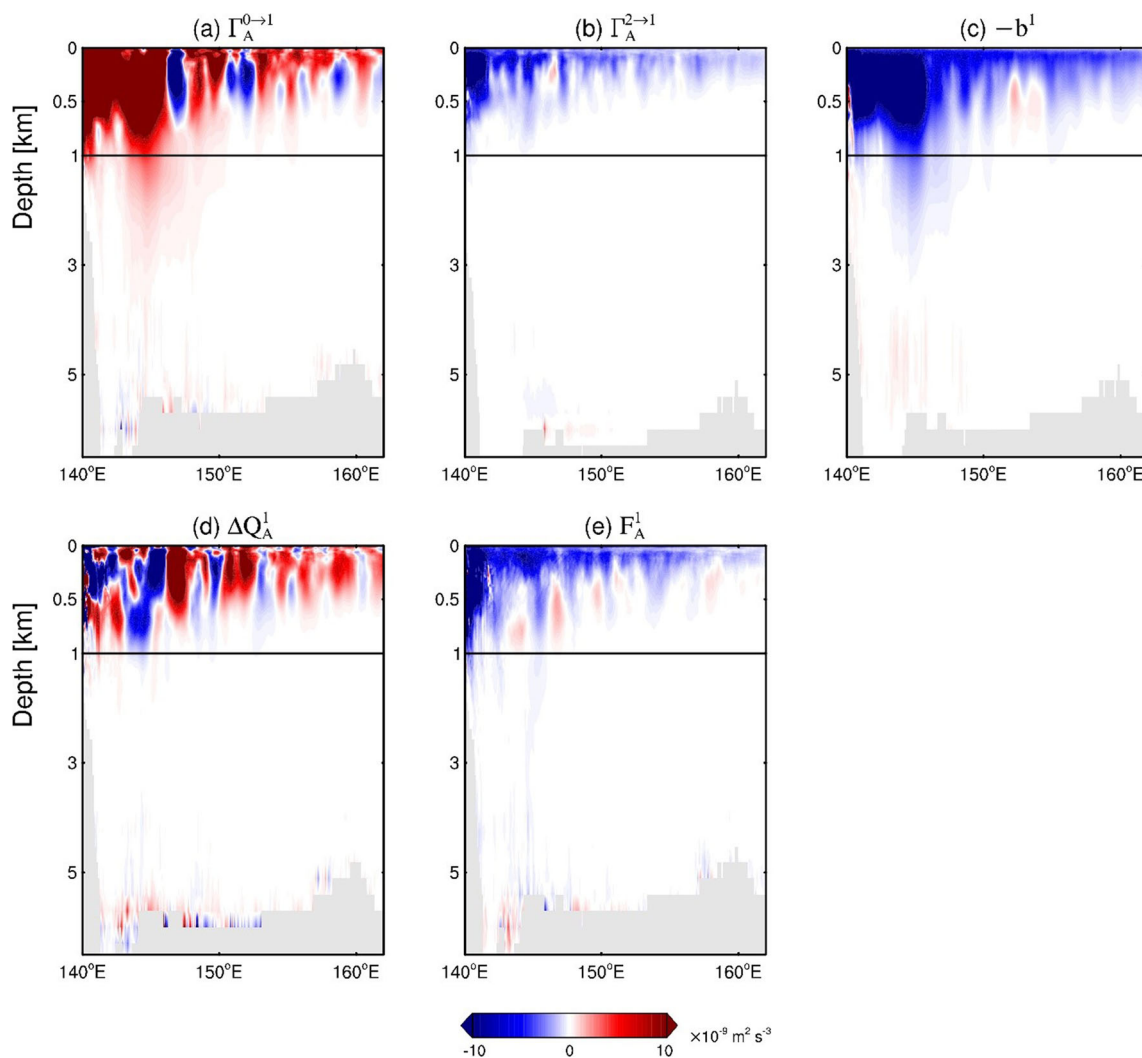


Fig. 4 Time-mean (1993–2009) depth-longitude sections of the A^1 budget terms ($10^{-9} \text{ m}^2 \text{ s}^{-3}$) averaged along the $32^\circ\text{--}38^\circ\text{N}$ band, showing (a) $\Gamma_A^{0\rightarrow 1}$, (b) $\Gamma_A^{2\rightarrow 1}$, (c) $-b^1$, (d) ΔQ_A^1 , and (e) F_A^1 . The S_A^1 term is negligible and thus is not shown. In these subfigures, a pixel is identified as seafloor

topography (in gray) only if there are no valid grids between the averaging longitudinal band. The different seafloor topography appearing in each subfigure is due to the interpolation from original B-grid fields produced by the OFES2 model

To better understand the above results, we check the necessary condition for the baroclinic instability by calculating the cross-stream gradient of Ertel’s potential vorticity (PV) at three latitudinal transections (142.5°E , 146°E , and 152°E) where the mean flow is roughly zonal. The Ertel PV Q is defined as:

$$Q = -\frac{1}{\rho_0} (2\Omega + \nabla \times \mathbf{v}) \cdot \nabla \rho_\theta, \tag{9}$$

where 2Ω is the vector of Earth’s rotation velocity and ρ_θ is the potential density (Ertel 1942). From Fig. 6, it can be seen that the time-mean (1993–2009) PV gradient (Q_y) sign reversal occurs near the jet axis in the 200–700-m depth range, at all three sections, suggesting that the upper layer jet meets the necessary condition for baroclinic instability. These results

agree with the dominant positive baroclinic canonical transfers as shown in Fig. 4a.

Besides the dominant negative $-b^1$, APE transfer from the intraseasonal variability to the higher-frequency synoptic variability (negative $\Gamma_A^{2\rightarrow 1}$; Fig. 4b) and diffusion processes (negative F_A^1 ; Fig. 4e) also acts to dissipate A^1 , but their effects are only confined within the upper 1000 m. The nonlocal term ΔQ_A^1 exhibits a more complex spatial structure than other terms in the A^1 budget equation, with alternating positive and negative signals from upstream to downstream (Fig. 4d). There are strong negative ΔQ_A^1 signals west of 146°E and positive signals east of 146°E , implying that the intraseasonal APE is advected from the upstream region of eddy generation from baroclinic instability to the downstream region.

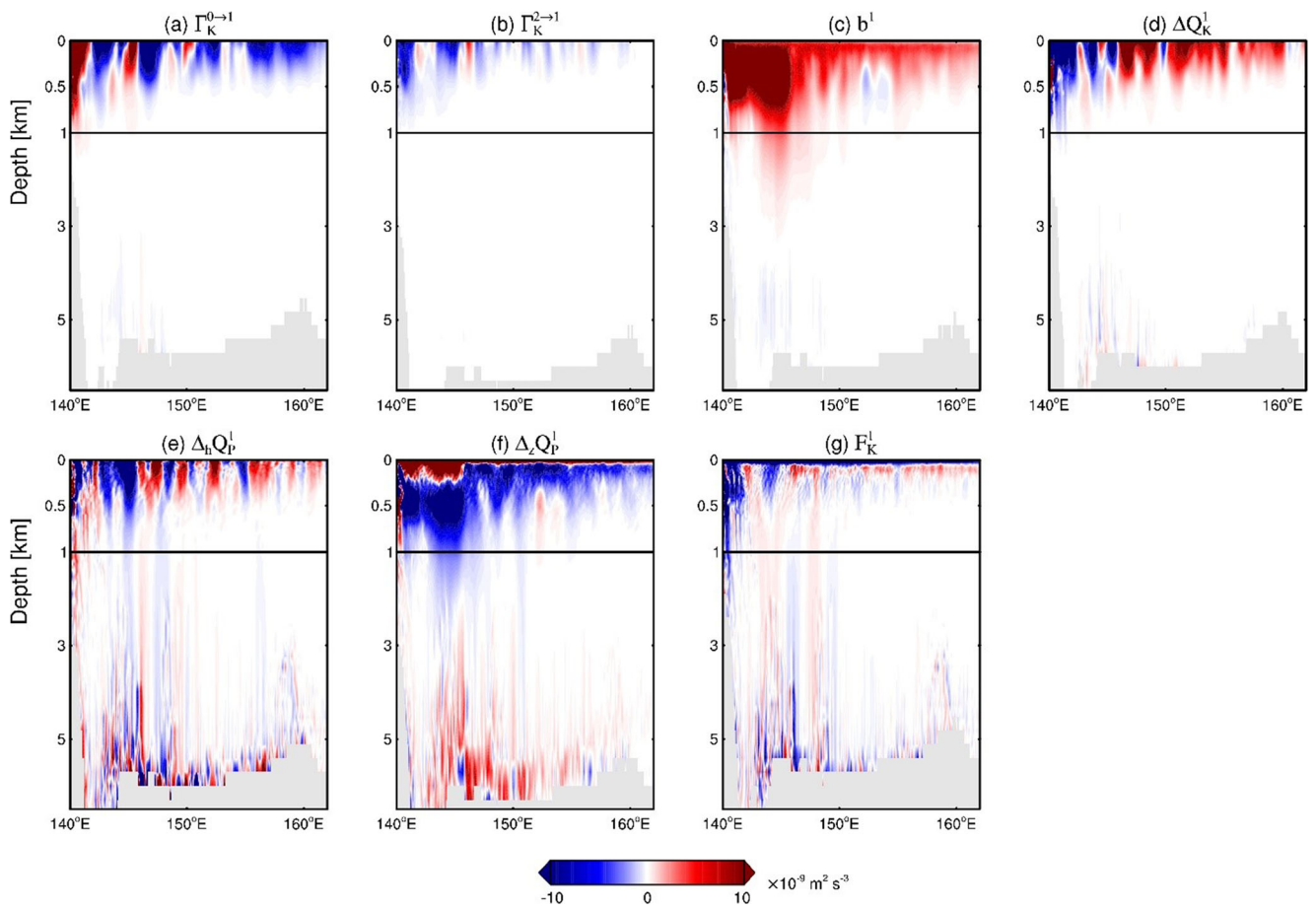


Fig. 5 As in Fig. 4, but for the the K^1 budget terms, showing (a) $\Gamma_K^{0\rightarrow 1}$, (b) $\Gamma_K^{2\rightarrow 1}$, (c) b^1 , (d) ΔQ_K^1 , (e) $\Delta_h Q_P^1$, (f) $\Delta_z Q_P^1$, and (g) F_K^1

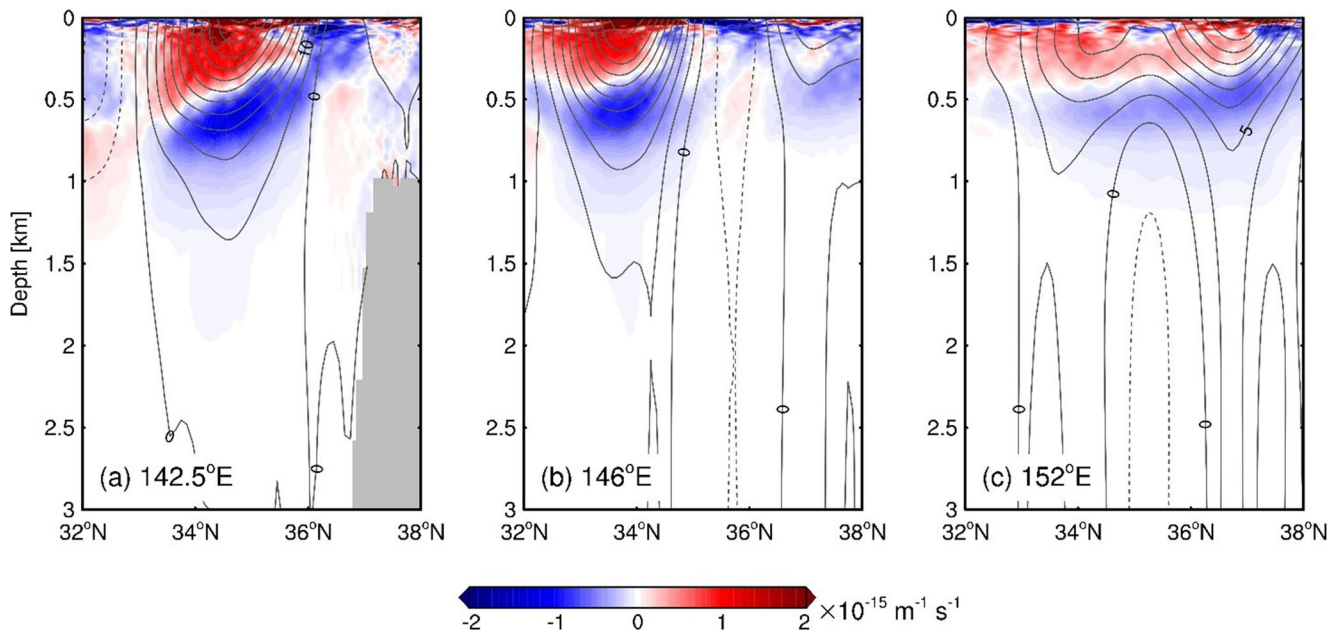


Fig. 6 Time-mean (1993–2009) vertical sections of cross-stream gradient of Ertel PV (color shading; $10^{-15} \text{ m}^{-1} \text{ s}^{-1}$), with zonal velocity (gray contours; cm s^{-1}) at (a) 142.5°E , (b) 146°E , and (c) 152°E

For the water column below 3000 m, the baroclinic instability energy route as found in the upper layer no longer exists. For instance, K^1 is seen to be weakly converted to A^1 between 4000 and 5500 m (i.e., positive $-b^1$), where the baroclinic transfer $\Gamma_A^{0 \rightarrow 1}$ is almost negligible (Fig. 4a and 4c). It is also interesting to note that the A^1 terms in the deep layer generally have a lower magnitude than the K^1 terms (Fig. 4 and 5). Several recent model-based studies have shown a similar feature in the deep Gulf of Mexico (e.g., Yang et al. 2020; Maslo et al. 2020). This feature is likely due to the fact that deep layer generally has a more flattened stratification than the upper layer and therefore has a smaller APE reservoir and associated transfers and conversions.

The vertical distribution of K^1 budget is shown in Fig. 5. The dominant KE source for the intraseasonal variability above 3000 m is from the positive buoyancy conversion b^1 , which has been shown as the major sink of the A^1 reservoir. Interestingly, the canonical KE transfer $\Gamma_K^{0 \rightarrow 1}$ is overwhelmingly negative, especially in the downstream region east of 146°E (Fig. 5a), indicating that intraseasonal KE is transferred back to the low-frequency background flow there. There are strong positive $\Gamma_K^{0 \rightarrow 1}$ nearshore around 140°E and 145°E, implying that these are the regions of intraseasonal eddy generation via barotropic instability. The above analysis on the canonical transfers from barotropic and baroclinic instabilities in the upper layer suggests that baroclinic instability plays a key role in generating the intraseasonal variability in the Kuroshio Extension. Previously, a multiscale interaction analysis of the mean, interannual, and eddy flows in Yang and Liang (2016) showed that eddies are generated via mixed barotropic–baroclinic instabilities in the upstream Kuroshio Extension. Different from the present study which focuses on eddy variability on the intraseasonal time scale, the eddy field in Yang and Liang (2016) is defined as processes with periods shorter than 1 year that includes contributions from not only high-frequency perturbations such as the intraseasonal and synoptic eddies but also the low-frequency motions like quasi-stationary meanders and long-lived mesoscale eddies. The latter has been shown to account for a significant portion of the total KE reservoir in this region (Fig. 1). The distinct instability features as revealed in Yang and Liang (2016) and this study indicate that mesoscale variability at different time scales could be generated by different mechanisms.

The vertical pressure work $\Delta_z Q_p^1$ exhibits a very distinct structure of alternating positive and negative signals in the vertical direction (Fig. 5f). West of 146°E, $\Delta_z Q_p^1$ is positive above 200 m, negative between depths of 200 m and 3000 m, and again positive below 3000 m. East of 146°E, the surface positive $\Delta_z Q_p^1$ is merely limited at depths shallower than ~ 50 m. Recall that the regions with strong negative $\Delta_z Q_p^1$ are also regions with strong baroclinic production of K^1 , indicating that the vertical pressure work serves as the dominant sink of K^1 in

the ocean interior. The positive signals above and beneath the negative layer of $\Delta_z Q_p^1$ imply that K^1 is transported both upward and downward. To further confirm the role of the vertical pressure work in redistributing the intraseasonal KE in the water column, we plot the vertical component of the intraseasonal eddy pressure flux, i.e., $\widehat{w}^{-1} \widehat{P}^{-1} / \rho_0$, in Fig. 7. As expected, the pressure flux is dominantly downward (upward) beneath (above) ~ 200 m, except in the near-shore region (east of 146°E) where intense upward pressure flux is seen in the upper 1000 m. Due to the boundary constraint at the surface and the seafloor, such pattern of vertical energy flux leads to a convergence of energy at the surface and the abyss, and a divergence of energy in the ocean interior, corresponding to the vertical distribution of $\Delta_z Q_p^1$ as shown in Fig. 5f. The above results highlight the important role of vertical pressure work in redistributing the intraseasonal EKE among the ocean surface, interior and deep layers.

With a focus on the Gulf Stream region, several previous studies suggested that baroclinic instability is the primary mechanism for the growth of the upper meander and deep cyclogenesis via stretching of the deep water column (e.g., Savidge and Bane 1999; Kämpf 2005). Similar processes have also been found in the deep Kuroshio Extension (Greene et al. 2012), although the deep eddy intensification in this region generally begins from externally generated finite-amplitude perturbations (Greene et al. 2012; Bishop 2013). In these studies, the intensification of the deep variability is explained by the perspective of PV conservation, or the conservation of angular momentum. In this study, we attempt to provide some perspective from an energetics point of view. As shown above, positive baroclinic energy transfer dominantly occurs in the upper layer that generating intraseasonal eddy energy which is then transported downward into the deep layer via pressure work. Our result highlights the role of pressure work in bridging the energetics of the upper and deep layers in the Kuroshio Extension region. It is possible that the vortex tube stretching mechanism, as proposed in previous studies, and vertical pressure work are about the same physical process with different perspectives, which could be the object of future research.

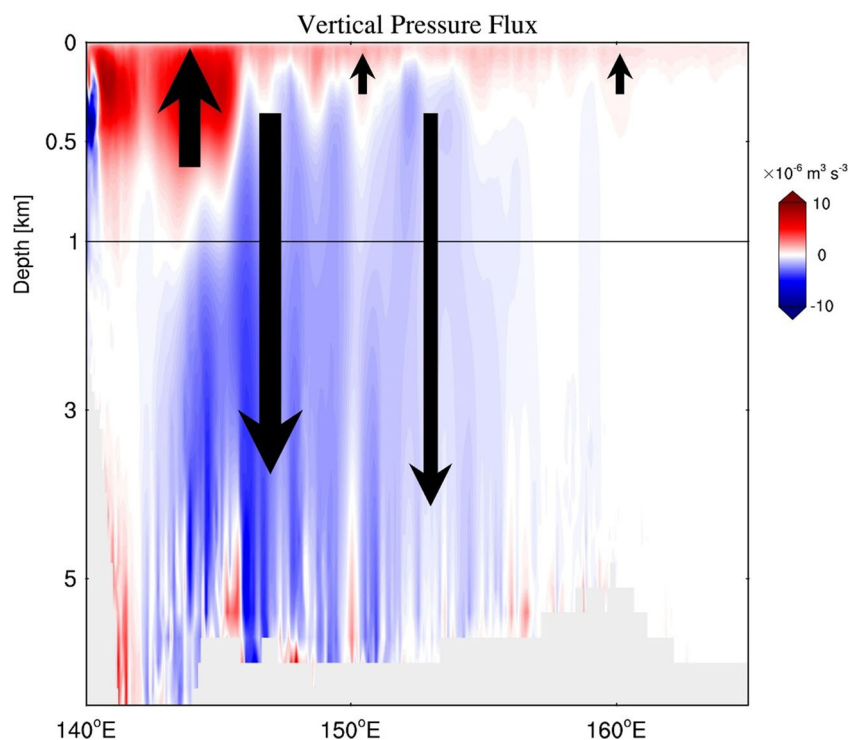
In the downstream region of the upper layer Kuroshio Extension (i.e., east of 146°E), advection also serves as a comparable KE source for the intraseasonal variability as baroclinic instability (Fig. 5d). The spatial feature of the advection term ΔQ_K^1 , i.e., negative upstream and positive downstream, implies that the K^1 is transported downstream by the eastward background flow. The KE transfer between the intraseasonal variability and synoptic (i.e., < 30 days) variability is relatively weak in a forward sense (i.e., negative $\Gamma_K^{2 \rightarrow 1}$), indicating that the high-frequency motions mainly act to extract energy from the intraseasonal KE reservoir. The horizontal redistribution by the pressure work $\Delta_h Q_p^1$ displays positive and negative signals in the upper layer. As will be discussed

later, the net contribution of this process is negative in the upper ocean, showing that the intraseasonal KE is radiated away from the jet, possibly in a form of nonlinear transient Rossby waves (Tai and White 1990). The F_K^1 term exhibits strong negative values at the ocean surface as well as in the lee of topography around 140°E (i.e., the Izu–Ogasawara Ridge). Note that this term is treated as a residue term in Eq. (7) so that it includes external forcings such as wind stress, bottom stress, and internal turbulent dissipations. Considering that small-scale (such as submesoscale) processes are not resolved by the present 1/10° model, some candidate-dissipating processes such as submesoscale instabilities and boundary mixing can be ruled out for explanation of the negative F_K^1 diagnosed from the model simulation. Therefore, the surface intensified negative F_K^1 is more likely to be a result of eddy energy damping by wind stress, consistent with the well-recognized “relative wind stress effect”, which states that atmospheric wind tends to remove KE from the eddy currents with respect to the current feedback on the surface wind stress (e.g., Hughes and Wilson 2008; Xu et al. 2016; Yang et al. 2021). This mechanism is well-presented in eddy-resolving coupled atmosphere–ocean models and ocean-only models (such as the OFES2 model) with the relative motion between the wind stress and underlying ocean current taken into account. Another spot of high damping rate is found in the lee of the Izu–Ogasawara Ridge. This feature is consistent with the large vertical diffusivity over rough bottom topography produced by the local mixing scheme in OFES2 (Sasaki et al., 2020).

It is interesting to note that in the upper layer, almost all K^1 terms are of the same magnitude, while in the deep layer, only the $\Delta_h Q_p^1$, $\Delta_z Q_p^1$, and F_K^1 terms are important (see Fig. 5e–g). The overwhelming positive and bottom intensified pattern of $\Delta_z Q_p^1$ as found in the deep layer suggests a significant nonlocal energy pathway for the intraseasonal variability transporting from the upper layer to the deep layer. In contrast, $\Delta_h Q_p^1$ displays a rather noisy spatial pattern in the deep layer (Fig. 5e). As will be seen later, the area mean of this term is negligible, showing that the horizontal pressure work does not serve as a dominant energy source for the deep intraseasonal variability. To keep balance, the residue term F_K^1 shows overall negative values in the deep basin (Fig. 5g), implying that strong turbulent dissipation occurs near the ocean floor through the bottom drag.

The important role played by the vertical pressure work in eddy energy redistribution between upper and lower layers has been systematically investigated by Zhai and Marshall (2012). They found distinct vertical eddy energy flux pattern in the subtropical, western boundary (i.e., Gulf Stream), and subpolar regions of the North Atlantic Ocean. Specifically, in the subtropical gyre and western boundary, the eddy generation by baroclinic instability is located near the surface, and the vertical eddy energy flux is downward. In contrast, in the subpolar gyre, the eddy generation is deep down, and the vertical eddy energy flux is found to be upward. The downward vertical pressure flux from the upper layer to deep layer as found in the Kuroshio Extension is similar to that in the

Fig. 7 Time-mean (1993–2009) depth–longitude sections of the vertical intraseasonal eddy pressure flux $\frac{1}{\rho_0} \widehat{w}^{-1} \widehat{P}^{-1}$ ($10^{-3} \text{ m}^2 \text{ s}^{-2}$) averaged along the 32°–38°N band



Gulf Stream as reported by Zhai and Marshall (2012), indicating a universal dynamics that deep eddies are powered by energy transporting from the upper layer. Despite this similarity, from our study, some differences between the energy pathways in these two western boundary current regions are noticeable. For example, we have found a significant upward pressure flux in the surface mixed layer of the upstream Kuroshio Extension (above ~ 200 m, west of 146°E), where contribution from the pressure work can even exceed that from the baroclinic instability pathway. Such upward eddy energy flux feature is not observed in the Gulf Stream (see Fig. 6 in Zhai and Marshall 2012). Besides, our energetics analysis also highlights the importance of nonlocal sources of eddy energy in the downstream Kuroshio Extension (east of 146°E); that is, the KE source for the intraseasonal perturbation in the surface layer of the downstream region mainly comes from horizontal advection from the upstream. The along-stream variation of the energy pathway was not shown in Zhai and Marshall (2012). As will be seen soon, to distinguish this prominent along-stream variation, the Kuroshio Extension needs to be divided into two horizontal subdomains for an appropriate analysis.

3.3 Vertical coupling of the energy pathway among different layers

According to the vertical structure of $\Delta_z Q_p^1$, we divide the water column of the Kuroshio Extension into three vertical layers, namely, the surface layer (0–230 m), the interior layer (230–3000 m), and the deep layer (3000–5700 m), to examine how the dynamics of the intraseasonal variability among these layers are coupled. Note that the values of APE and APE-related terms depend largely on the definition of the reference stratification. For depths deeper than 5700 m, we find that the reference buoyancy frequency squared, N^2 , becomes negative and hence no APE can be defined based on it. This is because there are not enough grid points to define a stable reference stratification below 5700 m. To avoid such issue, we limit the bottom of the deep layer as the depth of 5700 m in this study. To further distinguish the along-stream variation of the energy pathway, we divide the Kuroshio Extension into two horizontal subdomains, namely, the upstream region (142°–146°E, 32°–38°N) and downstream region (146°–155°E, 32°–38°N). Fig. 8 shows the volume-integrated energy cycle diagrams for the six considered volumes. Since this study focuses on the intraseasonal variability, Fig. 8 only displays the energy flows related to the K^1 and A^1 reservoirs.

For the surface layer west of 146°E (Fig. 8a), the baroclinic transfer (positive $\Gamma_A^{0 \rightarrow 1}$) is the dominant source for the A^1 reservoir (account for ~ 97% of the total A^1 sources), while the buoyancy conversion (positive b^1), diffusion (negative F_A^1), forward temporal cascade toward high-frequency eddies

(negative $\Gamma_A^{2 \rightarrow 1}$), and advection (negative ΔQ_A^1) form the sinks for A^1 in this volume, which account for 39%, 26%, 18%, and 17% of the total A^1 sinks, respectively. Regarding the K^1 budget, $\Delta_z Q_p^1$ and b^1 are the sources for the upstream surface K^1 reservoir, which account for 67% and 33% of the total K^1 generation, while the $\Delta_h Q_p^1$, F_K^1 , and ΔQ_K^1 are the three dominant sinks for K^1 , accounting for 31%, 30%, and 22% of the K^1 dissipation in this volume. Distinctly different from the upstream region, the downstream (east of 146°E) K^1 reservoir in the surface layer mainly gains energy via lateral advection (i.e., positive ΔQ_K^1 ; see Fig. 8b). The incoming K^1 advection accounts for ~ 60% of the total K^1 sources in this volume, in contrast to the APE conversion (positive b^1) which accounts for 30% of the total K^1 sources. The negative ΔQ_K^1 ($39.2 \times 10^4 \text{ m}^5 \text{ s}^{-3}$) upstream and positive ΔQ_K^1 ($110.0 \times 10^4 \text{ m}^5 \text{ s}^{-3}$) downstream suggest that a significant portion of K^1 in the downstream region is advected from the upstream region. The dominant sinks for the downstream K^1 are the negative canonical transfer $\Gamma_K^{0 \rightarrow 1}$ (41%) and dissipation F_K^1 (41%). Notice that negative $\Gamma_K^{0 \rightarrow 1}$ is also an important damping mechanism for the upstream K^1 (see Fig. 5a), although the volume integral shows a relatively small value compared to the downstream counterpart, due to the offset of strong positive and negative values in the upstream region. The above energy diagram confirms the Charney-type baroclinic instability occurring in the surface ocean, that is, a well-established baroclinic instability pathway (i.e., $A^0 \rightarrow A^1 \rightarrow K^1$) and a strong inverse temporal cascade of KE (i.e., $K^1 \rightarrow K^0$). Interestingly, we find that the upward transport of K^1 by vertical pressure flux ($\Delta_z Q_p^1$) is larger than that generated via the baroclinic instability pathway at the surface layer of the upstream region (Fig. 8a). The horizontal distributions of these two processes in the surface layer are presented in Fig. 9a and 9b, respectively. One can see that a well-defined pool of positive $\Delta_z Q_p^1$ occupies the upstream region of the Kuroshio Extension (140°–146°E, 32°–38°N), where the first quasi-meander of the eastward jet is located. The baroclinic production of K^1 is dominantly positive over the whole region and has smaller values than $\Delta_z Q_p^1$ in the upstream. These results evidence the impact of the ocean interior on the surface eddy variability.

The energy pathway in the interior layer is less complex than that in the surface layer (Fig. 8c, d). In the upstream region of this layer, $\Gamma_A^{0 \rightarrow 1}$ and b^1 dominate the intraseasonal APE budget. $\Gamma_A^{0 \rightarrow 1}$ is the only process generating A^1 and b^1 accounts for ~ 73% for the total A^1 sinks (Fig. 8c). Based on the in situ data from the KESS project, Bishop (2013) estimated the eddy APE (EAPE) budget equation at 400 m and found an overall balance between the APE transfer from the background flow to the eddies and the buoyancy conversion from EAPE to EKE in this region. The similarity between the results of Bishop’s (2013) work and ours confirms a robust

baroclinic instability energy pathway occurring in the main thermocline of the upstream Kuroshio Extension. In contrast to the surface layer, the ocean interior, especially for the upstream Kuroshio Extension (Fig. 8c), has a rather weak inverse temporal KE cascade, leaving $\Delta_z Q_P^1$ as the major mechanism ($\sim 76\%$ for the upstream and 68% for the downstream) that removes the excess K^1 from this layer. The counterbalance of the K^1 generation by buoyancy conversion and dissipation by vertical pressure work is further illustrated by their

horizontal patterns in Fig. 9c and d. Besides the dominant removal role played by the vertical pressure work, the horizontal pressure work also contributes about 17% of the total upstream K^1 sinks, consistent with previous study (Tai and White 1990). Also different from the surface layer, the residue term F_K^1 and the canonical KE transfer toward high-frequency motions are small in magnitude, indicating that forward temporal cascade is inhibited in the ocean interior. Furthermore, the small amplitude outgoing EKE advection in the upstream

Fig. 8 Schematics of the intraseasonal energy budgets (volumn integration) over the upstream region (indicated as box 1 in Fig. 2) and downstream region of the Kuroshio Extension (indicated as box 2 in Fig. 2). The volume integration is taken for (a, b) the surface layer (0–230 m), (c, d) interior layer (230–3000 m), and (e, f) deep layer (3000–5700 m). The energy flows are all in units of $10^4 \text{ m}^5 \text{ s}^{-3}$

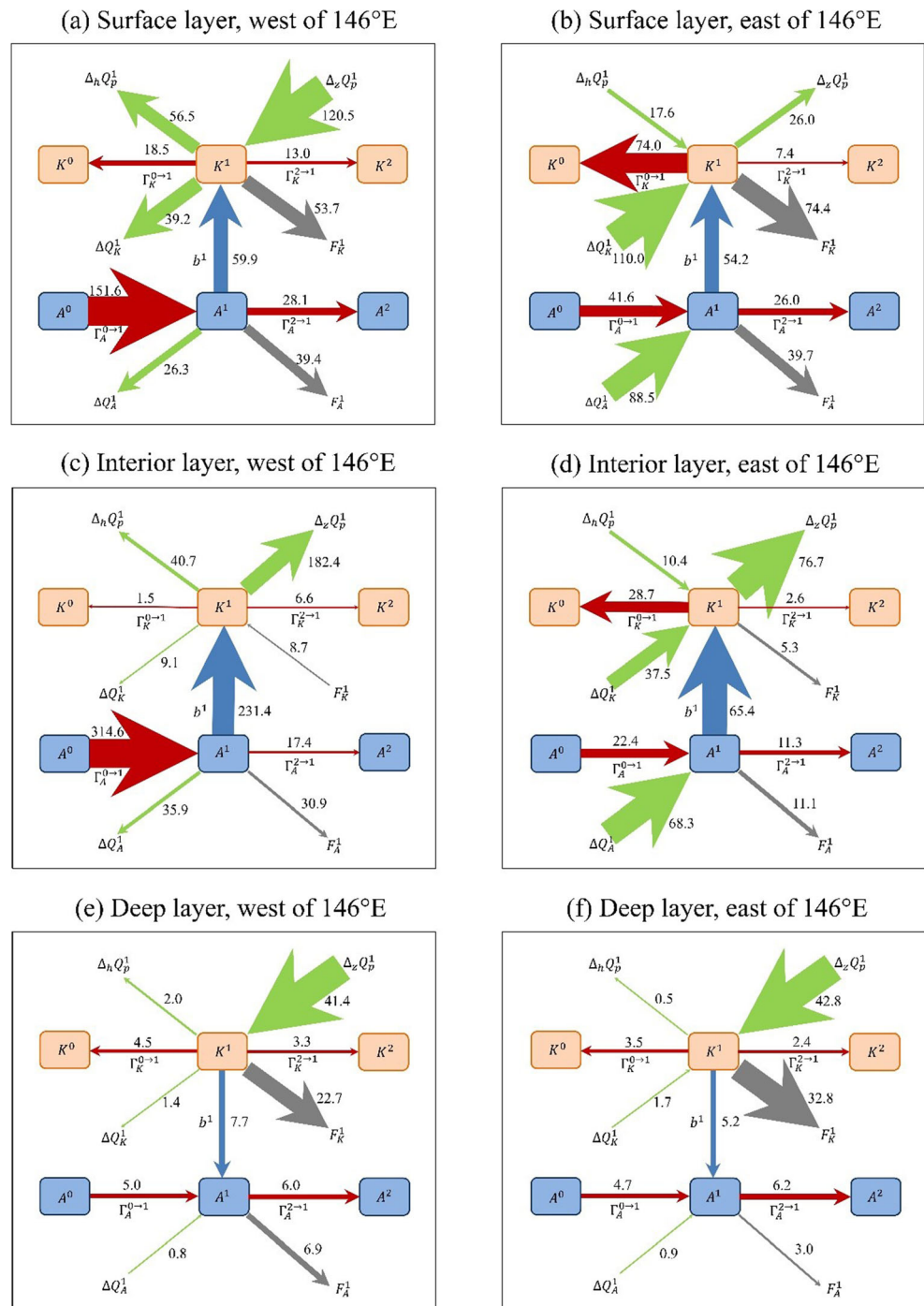
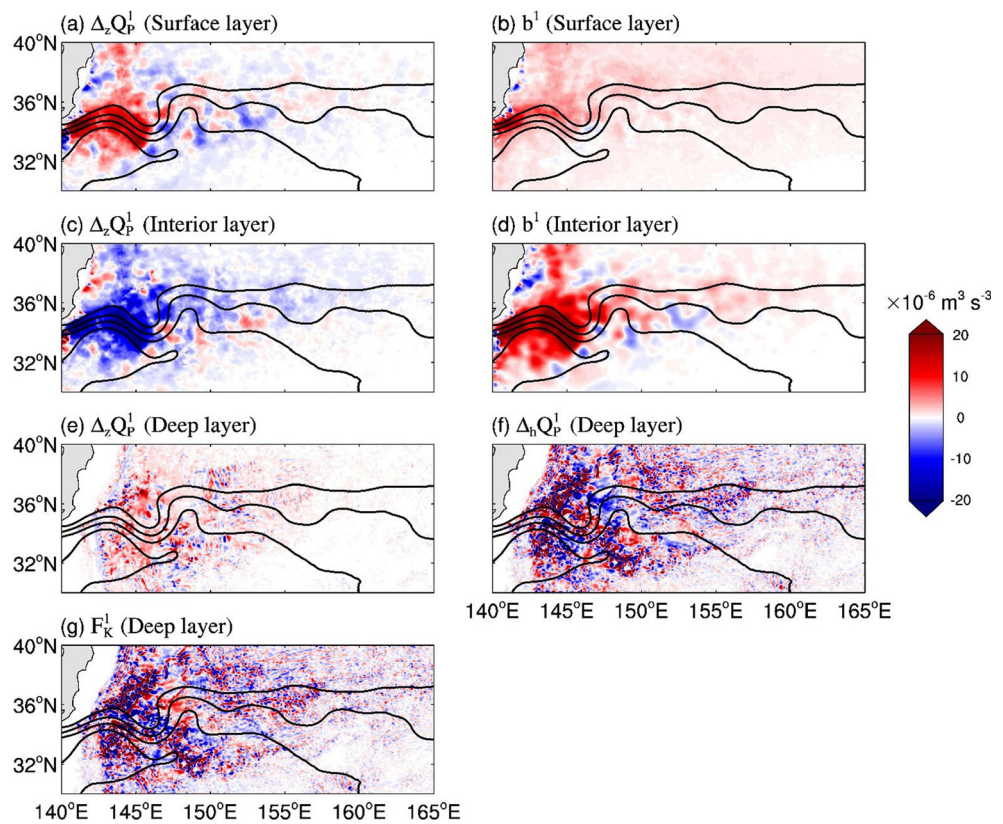


Fig. 9 Horizontal maps of the dominant energetic terms ($10^{-6} \text{ m}^3 \text{ s}^{-3}$) vertically integrated within different depths, showing (a) $\Delta_z Q_p^1$, (b) b^1 for the upper layer (0–230 m), (c) $\Delta_z Q_p^1$, and (d) b^1 for the interior layer (230–3000 m), and (e) $\Delta_z Q_p^1$, (f) $\Delta_h Q_p^1$, and (g) F_k^1 for the deep layer (3000–5700 m). The time mean (1993–2009) SSH is superposed with black contour in each figure



(Fig. 8c) suggests that the nonlocal EKE transport in the downstream region (Fig. 8d) does not simply come from the upstream. Note that the integral value of ΔQ_k^1 is highly dependent on the domain size, especially for an open system like the Kuroshio Extension.

In the deep layer (Fig. 8e, f), $\Delta_z Q_p^1$ contributes most of the total K^1 sources (100% for the upstream subdomain and 96% for the downstream subdomain), and the F_k^1 serves as the major mechanism that dissipates the deep K^1 (account for, respectively, 55% and 74% of the total K^1 dissipations in the upstream and downstream region). The inverse buoyancy conversion (i.e., $K^1 \rightarrow A^1$), KE transfers from the intraseasonal-scale flow to the background flow (i.e., $K^1 \rightarrow K^0$), and high-frequency eddies (i.e., $K^1 \rightarrow K^2$) are secondary dissipating mechanisms, accounting for about 19% (12%), 11% (8%), and 8% (5%) of the total K^1 sinks in the upstream (downstream) of this layer, respectively. Similar deep energy pathway with dominant downward EKE transport via pressure work in the presence of strong dissipation by bottom drag also has been reported recently in the deep Gulf of Mexico (Yang et al. 2020; Maslo et al. 2020) and the South China Sea (Cai and Gan 2021; Quan et al. 2021). Still, there is a noticeable difference between our work and these previous works. In these previous studies, the authors found that, although the role of buoyancy conversion is secondary, it still releases a

significant amount of eddy APE to EKE in the deep layers of the two ocean sectors. Here in the deep Kuroshio Extension, we find that the intraseasonal EKE is converted to the APE reservoir instead. It is worth noting that the volume integration of the canonical APE transfer $\Gamma_A^{0 \rightarrow 1}$ is positive ($A^0 \rightarrow A^1$) in the deep layer. However, the A^1 is not converted to K^1 in this layer as the scenario in the upper layers. This suggests that the baroclinic instability pathway ($A^0 \rightarrow A^1 \rightarrow K^1$) is not well-established in the deep Kuroshio Extension. In fact, from the vertical structures (below 3000 m) of these two processes (Fig. 4a, c), one can see that positive $\Gamma_A^{0 \rightarrow 1}$ signals are mainly confined within depths of 3000–3500 m where b^1 is much weaker, whereas positive $-b^1$ (i.e., negative b^1) signals are mainly confined within depths of 4000–5500 m, where $\Gamma_A^{0 \rightarrow 1}$ is much weaker. These results indicate that baroclinic energy pathway is not an energy source for the intraseasonal perturbations in the deep layer of the Kuroshio Extension; in other words, the deep layer intraseasonal variability is not locally generated. A recent modeling study by Schubert et al. (2018) also found a similar energy scenario in the deep Gulf Stream.

It should be noted that all energy terms presented in Fig. 8 are from a volume-integration and time-mean perspective. Processes with small values as presented in the energy cycle diagrams do not necessarily mean they are unimportant from a

local perspective. For instance, although the horizontal pressure work $\Delta_h Q_p^1$ is negligible in a space-integrated perspective, its value could be very large locally, which can be clearly seen from its horizontal distribution (Fig. 9f). Unlike $\Delta_z Q_p^1$ with overall positive values (Fig. 9e), $\Delta_h Q_p^1$ exhibits a rather noisy pattern with large magnitude and rapidly fluctuating signs in the deep layer. As a mechanism to locally balance the large magnitude of $\Delta_h Q_p^1$, the horizontal pattern of the bottom drag and turbulent viscous stress processes (F_K^1) also show strong localized signals (Fig. 9g). Nevertheless, the volume integrals of these terms tell us that the damping of the deep intraseasonal EKE is mainly fulfilled by F_K^1 , by virtue of bottom drags.

Finally, it is worth noting that the mechanical energy (both KE and APE) transfers from the intraseasonal-scale motion to the high-frequency synoptic motion for the six-layered volumes are all positive (Fig. 8), indicating that the high-frequency eddies act to damp the intraseasonal eddies through forward temporal cascade. Take the three layers of upstream domain for example, the forward cascades of KE (APE) account for about 7% (18%), 3% (6%), and 8% (44%) of the total intraseasonal KE (APE) sinks for the upper, interior, and deep layers, respectively. This suggests that scale interaction between the intraseasonal and synoptic eddies is more intense at the surface and bottom than the ocean's interior. However, it should be cautioned that the synoptic scale window in this study does not possess submesoscale motions due to the insufficient resolution of the OFES2 model. Accordingly, the downscale energy transfers from the intraseasonal-scale window to the synoptic scale window might not be realistic.

4 Summary

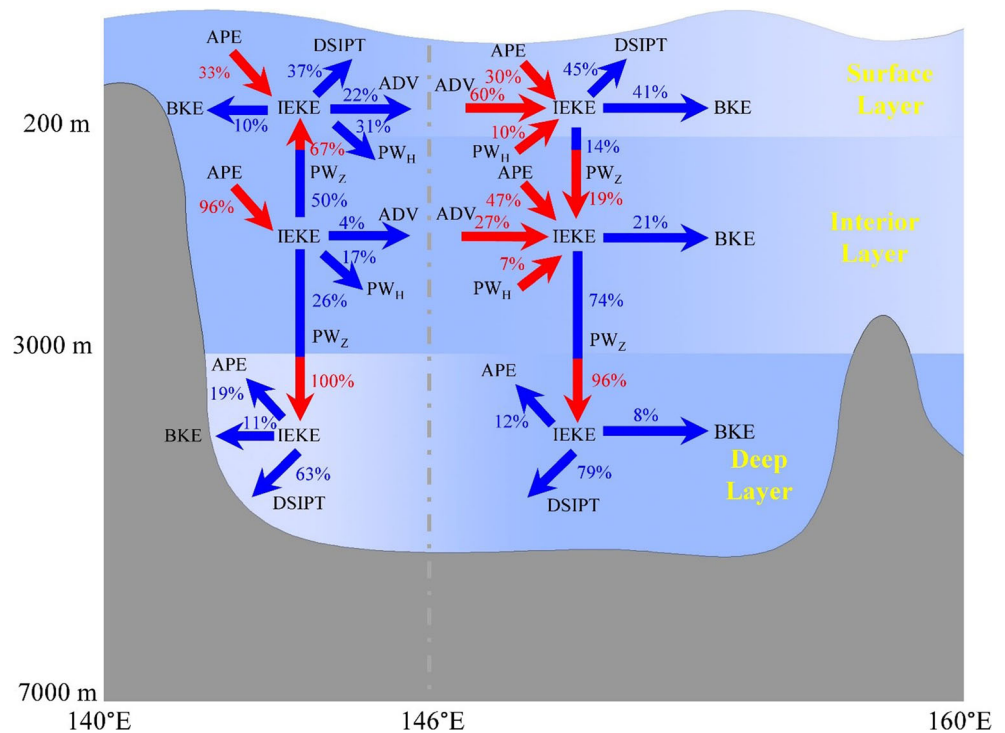
In situ observations and eddy-resolving model simulations have revealed substantial intraseasonal variability in the deep Kuroshio Extension (e.g., Greene et al. 2012; Bishop et al. 2012). Several previous studies have been conducted to understand the characteristics of the deep intraseasonal variability in this region and reported that these energetic features are associated with topographically controlled eddies, mainly in the form of topographic Rossby waves (TRWs) (e.g., Greene et al. 2012; Miyamoto et al. 2017). More importantly, a strong vertical coupling has been detected between the deep and upper currents in the intraseasonal band, from both observations and high-resolution simulations (e.g., OFES) (Tracey et al. 2012; Greene et al. 2012; Bishop 2013). But how the vertical coupling is fulfilled and what is the detailed dynamical causal relation between the vertical layers are still unknown. In this study, a three-scale energetics framework is employed to address this issue. Specifically, we have studied the multiscale dynamics associated with the intraseasonal

variability in the Kuroshio Extension, with a focus on the energy pathway that links the upper meandering western boundary current (WBC) and the deep mesoscale eddy flows. The multiscale system is reconstructed onto three temporal scale windows, namely, a slowly varying background flow window (periods > 90 days), an intraseasonal eddy window (30–90 days), and a high-frequency synoptic eddy window (< 30 days). The interactions among these windows and other energetics processes are investigated using the space-time-dependent energetics formalism by Liang and Robinson (2005, 2007) and the theory of canonical transfer (Liang 2016) based on the mathematical machinery multiscale window transform (MWT) (Liang and Anderson 2007). Particularly, the canonical transfer, which proves to have a Lie bracket form and conserves energy during multiscale interaction, gives a faithful quantification of the energy transfers among distinct scale windows, allowing us to investigate the multiscale interactions and instabilities in the Kuroshio Extension.

The three-dimensional energy pathway in the Kuroshio Extension is summarized in the schematic diagram in Fig. 10. The results show that typical baroclinic energy pathway (i.e., a transfer of APE from the background flow to the intraseasonal perturbations and then converted to EKE, denoted as $A^0 \rightarrow A^1 \rightarrow K^1$ in this study) is not well-established in the deep Kuroshio Extension (below 3000 m). Instead, a dominant nonlocal mechanism fulfilled by vertical pressure work is responsible to energize the intraseasonal currents in the abyssal ocean. Specifically, the vertical pressure work transports the intraseasonal KE to the deep layer (below 3000 m) from the interior layer (~200–3000 m) where baroclinic instability is the primary mechanism to extract APE from the low-frequency background flow to support the generation and growth of intraseasonal eddy variability. A budget analysis reveals that the excess intraseasonal KE in the deep ocean must be balanced by strong turbulent dissipation by virtue of bottom drags.

Besides the strong downward KE flux facilitated by pressure work, there is also a significant upward KE flux contributing to the development of intraseasonal variability in the surface mixed layer of the upstream Kuroshio Extension (above ~200 m, west of 146°E), where contribution from the pressure work can even exceed that from the baroclinic instability pathway. Different from the upstream, the KE source for the intraseasonal perturbation in the surface layer of the downstream region (east of 146°E) comes primarily from horizontal advection from the upstream and secondarily from baroclinic instability. The dissipation mechanisms of the intraseasonal KE are found to be different in the surface and interior layers. In the surface layer, the intraseasonal KE is mainly damped by wind stress and a significant inverse temporal cascade of KE toward lower-frequency flows. In contrast, the energy dissipation in the ocean's interior is featured by an overwhelming vertical divergence via pressure work.

Fig. 10 Schematic diagram of the intraseasonal energetics in the Kuroshio Extension. Percentages mean the contributions to the intraseasonal KE (IKE) from respective sources (in red font; represented by red arrows) and sinks (in blue font; represented by blue arrows). For clarity, only dominant processes are shown. Abbreviations used are as follows: DSIPT, dissipation (including the forward transfer from the intraseasonal-scale window to the synoptic-scale window and the residue term F_K^1); PW_H , horizontal pressure work; PW_Z , vertical pressure work; BKE, background kinetic energy; ADV, advection



The three-scale energetics framework also reveals that the higher-frequency synoptic eddies act to damp the intraseasonal variability through forward temporal cascades of KE and APE, and the forward cascades are found to be more intense near the surface and bottom than in the ocean interior. However, the energy transfers between the intraseasonal and synoptic scale windows are generally an order-of-magnitude smaller than the major terms, possibly due to the insufficient grid resolution of the present OFES2 model to resolve submesoscale motions. The spatial-temporal characteristics of the scale interaction between these two windows need future studies with highly resolved datasets.

This study provides a first attempt to investigate the energy pathway that links the intraseasonal variability in the upper and deep layers of the Kuroshio Extension system. Similar vertical coupling scenario of the energetics could also occur in other WBC regions, such as the eastern Gulf of Mexico (Yang et al. 2020). Our results highlight the importance of nonlocal sources of eddy energy in the ocean. The nonlocality occurs not only in the horizontal direction, for instance, via strong advection in the downstream region of the Kuroshio Extension, but also in the vertical direction, for instance, via upward/downward eddy pressure flux in the ocean surface and abyss. Finally, it should be noted that the vertical resolution of the present model is still too coarse below 3000 m (~ 200–300-m vertical grid spacing), which may lead to underestimated EKE in the deep ocean (e.g., Morey et al., 2020). Further modeling studies with higher vertical

resolution near the ocean’s bottom will provide insights on the dynamics of the deep circulations in this region.

Appendix

Multiscale window transform (MWT)

The Lorenz (1955) energy cycle theory has now been a standard approach to investigate the eddy-mean flow interaction and hydro-dynamical stability in atmosphere and ocean sciences (e.g., Böning and Budich 1992; Ivchenko et al. 1997; von Storch et al. 2012). The theory is based on Reynolds decomposition, with an ensemble mean (usually time mean in oceanic studies for practical reason) and its associated “eddy” component (i.e., deviation from the mean). Such decomposition results in four mechanical energy reservoirs, i.e., the kinetic energy (KE) and available potential energy (APE) for the mean flow and those for the eddy flow, and hence, energy exchanges among the four reservoirs can be quantitatively evaluated. It should be noted that the classical Lorenz energy cycle is formulated in a global form, and therefore is not suitable for investigation of energy burst processes which are in nature highly localized (i.e., nonstationary/inhomogeneous). A remedy for this is to use filter to separate a field into several parts and then take the square of the filtered part as the energy for that part. This practice, which has appeared trivially in a lot of publications (e.g., Hsu et al. 2011; Chapman et al. 2015), is

by no means trivial. To see why, suppose a time series $u(t)$ consists of two sinusoidal components with frequencies ω_0 and ω_1 (suppose $\omega_0 < \omega_1$), i.e.:

$$u(t) = \underbrace{(a_0 \cos \omega_0 t + b_0 \sin \omega_0 t)}_{\bar{u}(t)} + \underbrace{(a_1 \cos \omega_1 t + b_1 \sin \omega_1 t)}_{u'(t)}. \quad (10)$$

The energies for the low- and high-frequency component are the square of their respective transform coefficients, i.e., $a_0^2 + b_0^2$ and $a_1^2 + b_1^2$, which are obviously not equal to the square of the respective reconstructed (or filtered) fields, i.e., $[\bar{u}(t)]^2$ and $[u'(t)]^2$. From the above example, it is important to realize that transform coefficients, and hence multiscale energy, are concepts in phase space, while reconstructed fields are concepts in physical space. The two concepts are related through the Parseval equality. Particularly, when \bar{u} is a constant (i.e., time mean), it is easy to obtain $a_1^2 + b_1^2 = [\overline{u'(t)}]^2$. This explains why the time-averaging operator in the Reynolds-based energetics formalism cannot be simply removed.

So it is by no means a trivial problem to obtain a *localized* multiscale energy (here, *localized* means *time-dependent* since the decomposition is conducted in the time domain). General filters fail in the presentation of multiscale energy because they only yield reconstructions (filtered variables) but no transform coefficients. The multiscale window transform (MWT), developed by Liang and Anderson (2007), is used for this very purpose. Briefly speaking, MWT is a functional analysis tool that orthogonally decomposes a function space into a direct sum of subspaces, or *scale windows* as termed by Liang and Anderson (2007). Just like the Fourier transform and inverse transform pair, there exists a transform-reconstruction pair, which is the MWT and its peer, multiscale window reconstruction (MWR). For each MWR of a time series $u(t)$, denoted as $u^{\sim\varpi}(t)$, where ϖ indicates a specific scale window, there is a corresponding transform coefficient, denoted as $\hat{u}_n^{\sim\varpi}$ with n the discrete time step. The *time-dependent* energy on window ϖ proves to be the square of the MWT coefficients, i.e., $(\hat{u}_n^{\sim\varpi})^2$ (up to some constant; cf. Liang and Anderson 2007).

Canonical transfer

As we mentioned in Section 2.b, the MWT-based canonical transfer bears a conservation property which is not satisfied in classical Reynolds-based formalism. To see the difference between the canonical transfer and that appearing in the classical Reynolds-based formalism, consider a scalar field T in an incompressible flow v , with diffusion neglected for simplicity:

$$\frac{\partial T}{\partial t} + \nabla \cdot (vT) = 0. \quad (11)$$

By decomposing the original field into mean and eddy components, denoted by overbar and prime, respectively, one can obtain the energy equations for the mean and the eddy fields:

$$\frac{\partial}{\partial t} \left(\frac{1}{2} \overline{T^2} \right) + \nabla \cdot \left(\frac{1}{2} \overline{vT^2} \right) = -\overline{T\nabla \cdot (v'T)}, \quad (12)$$

$$\frac{\partial}{\partial t} \left(\frac{1}{2} T'^2 \right) + \nabla \cdot \left(\frac{1}{2} v'T'^2 \right) = -\overline{v'T'} \cdot \nabla \overline{T}, \quad (13)$$

where the second terms on the left-hand side of Eqs. (12) and (13) are the nonlocal transport processes by advection, and the terms on the right-hand sides are considered as energy transfers associated with eddy-mean flow interactions. It is important to note that the two terms on right-hand sides generally do not cancel out, meaning that the so-obtained transfer does not conserve energy among scales. This problem is actually not new and has long been realized that the transfer might not have a unique expression (e.g., Holopainen 1978; Plumb 1983). Based on MWT, Liang (2016) derived the energy equations for the special case (11):

$$\frac{\partial}{\partial t} \left(\frac{1}{2} \overline{T'^2} \right) + \nabla \cdot \left(\frac{1}{2} \overline{vT'^2} + \frac{1}{2} \overline{T v'T'} \right) = \Gamma. \quad (14)$$

$$\frac{\partial}{\partial t} \left(\frac{1}{2} \overline{T^2} \right) + \nabla \cdot \left(\frac{1}{2} \overline{vT^2} + \frac{1}{2} \overline{T v'T'} \right) = -\Gamma, \quad (15)$$

where the canonical transfer:

$$\Gamma = \frac{1}{2} \left[\overline{T\nabla \cdot (v'T')} - \overline{v'T'} \cdot \nabla \overline{T} \right]. \quad (16)$$

Now the transfer terms on the right-hand sides of Eqs. (14) and (15) sum to zero, distinctly different from the classical ones. As a validation, Liang and Robinson (2007) showed that, for a benchmark barotropic model whose instability structure is analytically known, the traditional formalism fails to give the correct source of barotropic instability, while canonical transfer Γ does.

Acknowledgements This is a paper in honor of Prof. Dr. Richard J. Greatbatch. Thanks are due to two anonymous referees for their valuable suggestions. YY thanks Qi Quan for valuable discussions and Mingming Bi for helping draw Fig. 10. OFES2 was conducted using the Earth Simulator under the support of JAMSTEC. YY and XSL are supported by the National Science Foundation of China (NSFC Grants 41806023, and 41975064), 2015 Jiangsu Program of Entrepreneurship and Innovation Group, Natural Science Foundation of the Higher Education Institutions of Jiangsu Province (18KJB170019).

Data availability OFES2 model output is available online (http://www.jamstec.go.jp/ofes/ofes_terms.html)

Code availability The energetics analysis package is available at <http://www.ncoads.org>.

Declarations

Conflict of interest The authors declare no competing interests.

References

- Bishop SP (2013) Divergent eddy heat fluxes in the kuroshio extension at 144°–148°E. Part II: Spatiotemporal Variability. *J Phys Oceanogr* 43:2416–2431. <https://doi.org/10.1175/JPO-D-13-061.1>
- Bishop SP, Bryan FO (2013) A comparison of mesoscale eddy heat fluxes from observations and a high-resolution ocean model simulation of the Kuroshio Extension. *J Phys Oceanogr* 43:2563–2570. <https://doi.org/10.1175/JPO-D-13-0150.1>
- Bishop SP, Watts DR, Park J-H, Hogg NG (2012) Evidence of bottom-trapped currents in the Kuroshio Extension region. *J Phys Oceanogr* 42:321–328. <https://doi.org/10.1175/JPO-D-11-0144.1>
- Böning CW, Budich RG (1992) Eddy dynamics in a primitive equation model: sensitivity to horizontal resolution and friction. *J Phys Oceanogr* 22:361–381. [https://doi.org/10.1175/1520-0485\(1992\)022<0361:EDIAPE>2.0.CO;2](https://doi.org/10.1175/1520-0485(1992)022<0361:EDIAPE>2.0.CO;2)
- Cai Z, Gan J (2021) Dynamics of the layered circulation inferred from kinetic energy pathway in the South China Sea. *J Phys Oceanogr* 51:1671–1685. <https://doi.org/10.1175/JPO-D-20-0226.1>
- Chapman CC, McC A, Hogg A, Kiss E, Rintoul SR (2015) The dynamics of southern ocean storm tracks. *J Phys Oceanogr* 45:884–903. <https://doi.org/10.1175/JPO-D-14-0075.1>
- Dewar WK, Bane JM (1989) Gulf stream dynamics. Part II: Eddy Energetics at 73°W. *J Phys Oceanogr* 19:1574–1587. [https://doi.org/10.1175/1520-0485\(1989\)019<1574:GSDPIE>2.0.CO;2](https://doi.org/10.1175/1520-0485(1989)019<1574:GSDPIE>2.0.CO;2)
- Donohue KA, Watts DR, Tracey KL, Greene AD, Kennelly M (2010) Mapping circulation in the Kuroshio Extension with an array of current and pressure recording inverted echo sounders. *J Atmos Ocean Technol* 27:507–527. <https://doi.org/10.1175/2009JTECH0686.1>
- Ertel H (1942) Ein neuer hydrodynamischer Erhaltungssatz. *Naturwissenschaften* 30:543–544. <https://doi.org/10.1007/BF01475602>
- Greatbatch RJ, Zhai X, Kohlmann J-D, Czeschel L (2010) Ocean eddy momentum fluxes at the latitudes of the Gulf Stream and the Kuroshio extensions as revealed by satellite data. *Ocean Dyn* 60:617–628. <https://doi.org/10.1007/s10236-010-0282-6>
- Greene AD, Sutyryn GG, Watts DR (2009) Deep cyclogenesis by synoptic eddies interacting with a seamount. *J Mar Res* 67:305–322. <https://doi.org/10.1357/002224009789954775>
- Greene AD, Watts DR, Sutyryn GG, Sasaki H (2012) Evidence of vertical coupling between the Kuroshio Extension and topographically controlled deep eddies. *J Mar Res* 70:719–747. <https://doi.org/10.1357/002224012806290723>
- Holmes RM, Thomas LN (2016) Modulation of tropical instability wave intensity by equatorial Kelvin waves. *J Phys Oceanogr* 46:2623–2643. <https://doi.org/10.1175/JPO-D-16-0064.1>
- Holopainen EO (1978) A diagnostic study of the kinetic energy balance of the long-term mean flow and the associated transient fluctuations in the atmosphere. *Geophysica* 15:125–145
- Hsu P, Li T, Tsou C-H (2011) Interactions between boreal summer intraseasonal oscillations and synoptic-scale disturbances over the western north Pacific. Part I: Energetics Diagnosis. *J Clim* 24:927–941. <https://doi.org/10.1175/2010JCLI3833.1>
- Hughes CW, Wilson C (2008) Wind work on the geostrophic ocean circulation: an observational study of the effect of small scales in the wind stress. *J Geophys Res Oceans* 113:C02016. <https://doi.org/10.1029/2007JC004371>
- Ivchenko VO, Treguier AM, Best SE (1997) A kinetic energy budget and internal instabilities in the fine resolution antarctic model. *J Phys Oceanogr* 27:5–22. [https://doi.org/10.1175/1520-0485\(1997\)027<0005:AKEBAI>2.0.CO;2](https://doi.org/10.1175/1520-0485(1997)027<0005:AKEBAI>2.0.CO;2)
- Jayne SR, Laurent LCS (2001) Parameterizing tidal dissipation over rough topography. *Geophys Res Lett* 28:811–814. <https://doi.org/10.1029/2000GL012044>
- Kämpf J, 2005: Cyclogenesis in the deep ocean beneath western boundary currents: a process-oriented numerical study. *J Geophys Res Oceans*, 110, <https://doi.org/10.1029/2003JC002206>.
- Large W, and Yeager S, 2004: Diurnal to decadal global forcing for ocean and sea-ice models: the data sets and flux climatologies. UCAR/NCAR,.
- Liang XS (2016) Canonical Transfer and multiscale energetics for primitive and quasigeostrophic atmospheres. *J Atmos Sci* 73:4439–4468. <https://doi.org/10.1175/JAS-D-16-0131.1>
- Liang XS, Robinson AR (2005) Localized multiscale energy and vorticity analysis: I. Fundamentals. *Dyn Atmos Oceans* 38:195–230. <https://doi.org/10.1016/j.dynatmoce.2004.12.004>
- Liang XS, Anderson DGM (2007) Multiscale window transform. *Multiscale Model Simul* 6:437–467. <https://doi.org/10.1137/06066895X>
- Liang XS, Robinson AR (2007) Localized multi-scale energy and vorticity analysis: II. Finite-amplitude instability theory and validation. *Dyn Atmos-Ocean* 44:51–76. <https://doi.org/10.1016/j.dynatmoce.2007.04.001>
- Lorenz EN (1955) Available potential energy and the maintenance of the general circulation. *Tellus* 7:157–167. <https://doi.org/10.1111/j.2153-3490.1955.tb01148.x>
- Mak M, Cai M (1988) Local barotropic instability. *J Atmos Sci* 46:3289–3311. [https://doi.org/10.1175/1520-0469\(1989\)046<3289:LBI>2.0.CO;2](https://doi.org/10.1175/1520-0469(1989)046<3289:LBI>2.0.CO;2)
- Maslo A, de Souza JMAC, Pardo JS (2020) Energetics of the Deep Gulf of Mexico. *J Phys Oceanogr* 50:1655–1675. <https://doi.org/10.1175/JPO-D-19-0308.1>
- Miyamoto M, Oka E, Yanagimoto D, Fujio S, Mizuta G, Imawaki S, Kurogi M, Hasumi H (2017) Characteristics and mechanism of deep mesoscale variability south of the Kuroshio Extension. *Deep Sea Res Part Oceanogr Res Pap* 123:110–117. <https://doi.org/10.1016/j.dsr.2017.04.003>
- Morey SL et al (2020) Assessment of numerical simulations of deep circulation and variability in the Gulf of Mexico using recent observations. *J Phys Oceanogr* 50:1045–1064. <https://doi.org/10.1175/JPO-D-19-0137.1>
- Na H, Watts DR, Park J-H, Jeon C, Lee HJ, Nonaka M, Greene AD (2016) Bottom pressure variability in the Kuroshio Extension driven by the atmosphere and ocean instabilities. *J Geophys Res Oceans*, n/a-n/a. <https://doi.org/10.1002/2016JC012097>
- Noh Y, Kim HJ (1999) Simulations of temperature and turbulence structure of the oceanic boundary layer with the improved near-surface process. *J Geophys Res Oceans* 104:15621–15634. <https://doi.org/10.1029/1999JC900068>
- Nonaka M, Sasaki H, Taguchi B, Schneider N (2020) Atmospheric-driven and intrinsic interannual-to-decadal variability in the Kuroshio Extension jet and eddy activities. *Front Mar Sci* 7. <https://doi.org/10.3389/fmars.2020.547442>
- Pedlosky J, 1987: *Geophysical fluid dynamics*. 2nd ed. Springer-Verlag, 710 pp.
- Plumb RA (1983) A new look at the energy cycle. *J Atmos Sci* 40:1669–1688. [https://doi.org/10.1175/1520-0469\(1983\)040<1669:ANLATE>2.0.CO;2](https://doi.org/10.1175/1520-0469(1983)040<1669:ANLATE>2.0.CO;2)
- Qiu B (1995) Variability and energetics of the Kuroshio Extension and its recirculation gyre from the first two-year TOPEX data. *J Phys Oceanogr* 25:1827–1842. [https://doi.org/10.1175/1520-0485\(1995\)025<1827:VAEOTK>2.0.CO;2](https://doi.org/10.1175/1520-0485(1995)025<1827:VAEOTK>2.0.CO;2)

- Qiu B, Chen S (2005) Variability of the Kuroshio Extension jet, recirculation gyre, and mesoscale eddies on decadal time scales. *J Phys Oceanogr* 35:2090–2103. <https://doi.org/10.1175/JPO2807.1>
- Qiu B, Chen S (2010) Eddy-mean flow interaction in the decadal modulating Kuroshio Extension system. *Deep Sea Res Part II Top Stud Oceanogr* 57:1098–1110. <https://doi.org/10.1016/j.dsr2.2008.11.036>
- Qiu B, Chen S, Klein P, Sasaki H, Sasai Y (2014) Seasonal mesoscale and submesoscale eddy variability along the North Pacific subtropical countercurrent. *J Phys Oceanogr* 44:3079–3098. <https://doi.org/10.1175/JPO-D-14-0071.1>
- Quan Q, Liu Z, Sun S, Cai Z, Yang Y, Jin G, Li Z, Liang XS (2021) Influence of the Kuroshio intrusion on deep flow intraseasonal variability in the northern South China Sea. *J Geophys Res Oceans*, n/a 126:e2021JC017429. <https://doi.org/10.1029/2021JC017429>
- Renault L, Masson S, Arsouze T, Madec G, McWilliams JC (2020) Recipes for how to force oceanic model dynamics. *J Adv Model Earth Syst* 12:e2019MS001715. <https://doi.org/10.1029/2019MS001715>
- Sasaki H, Nonaka M, Masumoto Y, Sasai Y, Uehara H, and Sakuma H, 2008: An eddy-resolving hindcast simulation of the quasiglobal ocean from 1950 to 2003 on the earth simulator. High resolution numerical modelling of the atmosphere and ocean, Springer, 157–185.
- Sasaki H, Klein P, Qiu B, Sasai Y (2014) Impact of oceanic-scale interactions on the seasonal modulation of ocean dynamics by the atmosphere. *Nat Commun* 5:1–8. <https://doi.org/10.1038/ncomms6636>
- Sasaki H et al (2020) A global eddying hindcast ocean simulation with OFES2. *Geosci Model Dev* 13:3319–3336. <https://doi.org/10.5194/gmd-13-3319-2020>
- Savidge DK, Bane JM (1999) Cyclogenesis in the deep ocean beneath the Gulf Stream: 2. *Dyn J Geophys Res Oceans* 104:18127–18140. <https://doi.org/10.1029/1999JC900131>
- Schubert R, Biastoch A, Cronin MF, Greatbatch RJ (2018) Instability-driven benthic storms below the separated Gulf Stream and the North Atlantic current in a high-resolution ocean model. *J Phys Oceanogr* 48:2283–2303. <https://doi.org/10.1175/JPO-D-17-0261.1>
- St. Laurent LC, Simmons HL, Jayne SR (2002) Estimating tidally driven mixing in the deep ocean. *Geophys Res Lett* 29:21-1–21–24. <https://doi.org/10.1029/2002GL015633>
- von Storch J-S, Eden C, Fast I, Haak H, Hernández-Deckers D, Maier-Reimer E, Marotzke J, Stammer D (2012) An estimate of the Lorenz energy cycle for the world ocean based on the STORM/NCEP simulation. *J Phys Oceanogr* 42:2185–2205. <https://doi.org/10.1175/JPO-D-12-079.1>
- Taguchi B, Xie S-P, Schneider N, Nonaka M, Sasaki H, Sasai Y (2007) Decadal variability of the Kuroshio Extension: observations and an eddy-resolving model hindcast. *J Clim* 20:2357–2377. <https://doi.org/10.1175/JCLI4142.1>
- Tai C-K, White WB (1990) Eddy variability in the Kuroshio Extension as revealed by geosat altimetry: energy propagation away from the jet, Reynolds stress, and seasonal cycle. *J Phys Oceanogr* 20:1761–1777. [https://doi.org/10.1175/1520-0485\(1990\)020<1761:EVITKE>2.0.CO;2](https://doi.org/10.1175/1520-0485(1990)020<1761:EVITKE>2.0.CO;2)
- Tracey KL, Watts DR, Donohue KA, Ichikawa H (2012) Propagation of Kuroshio extension meanders between 143° and 149°E. *J Phys Oceanogr* 42:581–601. <https://doi.org/10.1175/JPO-D-11-0138.1>
- Tsujino H et al (2018) JRA-55 based surface dataset for driving ocean–sea-ice models (JRA55-do). *Ocean Model* 130:79–139. <https://doi.org/10.1016/j.ocemod.2018.07.002>
- Wang Q, Tang Y, Pierini S, Mu M (2017) Effects of singular-vector-type initial errors on the short-range prediction of Kuroshio Extension transition processes. *J Clim* 30:5961–5983. <https://doi.org/10.1175/JCLI-D-16-0305.1>
- Wunsch C, Ferrari R (2004) Vertical mixing, energy, and the general circulation of the oceans. *Annu Rev Fluid Mech* 36:281–314. <https://doi.org/10.1146/annurev.fluid.36.050802.122121>
- Xu C, Zhai X, Shang X-D (2016) Work done by atmospheric winds on mesoscale ocean eddies. *Geophys Res Lett* 43:12,174–12,180. <https://doi.org/10.1002/2016GL071275>
- Yang H, Wu L, Chang P, Qiu B, Jing Z, Zhang Q, Chen Z (2021) Mesoscale energy balance and air–sea interaction in the Kuroshio Extension: low-frequency versus high-frequency variability. *J Phys Oceanogr* 51:895–910. <https://doi.org/10.1175/JPO-D-20-0148.1>
- Yang Y, Liang XS (2016) The instabilities and multiscale energetics underlying the mean–interannual–eddy interactions in the Kuroshio Extension region. *J Phys Oceanogr* 46:1477–1494. <https://doi.org/10.1175/JPO-D-15-0226.1>
- Yang Y, Liang XS (2018) On the seasonal eddy variability in the Kuroshio Extension. *J Phys Oceanogr* 48:1675–1689. <https://doi.org/10.1175/JPO-D-18-0058.1>
- Yang Y, Liang XS, Qiu B, Chen S (2017) On the decadal variability of the eddy kinetic energy in the Kuroshio Extension. *J Phys Oceanogr* 47:1169–1187. <https://doi.org/10.1175/JPO-D-16-0201.1>
- Yang Y, Weisberg RH, Liu Y, Liang XS (2020) Instabilities and multiscale interactions underlying the loop current eddy shedding in the Gulf of Mexico. *J Phys Oceanogr* 50:1289–1317. <https://doi.org/10.1175/JPO-D-19-0202.1>
- Zhai X, Marshall DP (2012) Vertical eddy energy fluxes in the north Atlantic subtropical and subpolar gyres. *J Phys Oceanogr* 43:95–103. <https://doi.org/10.1175/JPO-D-12-021.1>